Inclusion of a TKE Boundary Layer Parameterization in the Canadian Regional Finite-Element Model

R. BENOIT, J. CÔTÉ AND J. MAILHOT

Recherche en prévision numérique, Service de l'Environnement Atmosphérique, Dorval, Québec, Canada

(Manuscript received 31 May 1988, in final form 9 February 1989)

ABSTRACT

The formulation of the regional model recently implemented by the Atmospheric Environment Service of Canada for its operational 48 h NWP forecasts is presented. The emphasis is put on the parameterization of the physical processes, especially those affecting the atmospheric boundary layer. The originality of this model, in addition to the use of 3-D finite elements, of variable meshes in both the horizontal and vertical, and of being non-nested (as previously described by Staniforth and Daley), consists in the treatment of the time-dependent turbulent kinetic energy (TKE) and the inclusion of the full diurnal cycle. The overall organization of the model calculations is also presented in order to convey a more accurate description of this integrated system. Sample results from the well-known case of the Presidents' Day Cyclone of 1979 and general performance are covered in the last section.

1. Introduction

Keyser and Uccellini (1987) give an interesting interpretation of regional scale models (Anthes 1983) as being a new set of tools available to synoptic meteorologists. They relate the gradual emergence of regional models over the past 10 or 12 years, to the dual motivations of improving the real-time quantitative precipitation forecasting and of increasing our understanding of mesoscale phenomena. Thus, both operational constraints and research applications are generally intimately connected during the challenging exercise of developing a full-featured regional model. Our own case is certainly not an exception to this, since we wish to describe here the principal features of the Canadian regional finite-element (RFE) model. Since 22 April 1986, the RFE model is the prime model delivering Day 1 and Day 2 NWP forecasts to Environment Canada's forecast offices all across the country. Staniforth and Mailhot (1988) have recently discussed the original features of the RFE as a regional model adopting the variable resolution self-nesting strategy. This obviates the difficulties associated with more or less artificial lateral boundary conditions by the use of a large ($\approx$ hemispheric) total domain. The finite-element based numerical techniques employed throughout the model give a fourth order truncation error in the uniform grid area, are coded with high machine efficiency and provide a convenient mean to handle the variable resolution parts. It has been found that in practice the transition in resolution should be gradual (Staniforth and Mitchell 1978).

Ten years have elapsed since the description of a semi-implicit FE barotropic model by Staniforth and Mitchell (1977, 1978) which is the backbone of the full RFE model. A long evolution then followed, starting from the variable-resolution baroclinic (three-dimensional) FE model of Staniforth and Daley (1979, hereinafter referred to as SD) and leading to the current RFE model. Moisture was essentially a passive scalar in the 1979 version, without any surface evaporation, and the only condensation allowed was due to large-scale supersaturation or to a moist convective adjustment process. The only other physical forcing terms were a bulk surface friction (so-called Cressman drag) and a bulk heating due to the ocean surface temperature. At that time, a 285-km central-window resolution and 7-level configuration about equally distributed between roughly 10 kPa and surface, was tested extensively ($\sim$100 48-hour forecasts). It was found to be competitive with the then current operational spectral hemispheric model (5-level, rhomboidally truncated at wavenumber 29), and the authors concluded: "with the addition of a more sophisticated physics package and possibly a normal-mode initialization . . . [the RFE model] . . . will prove to be a very useful forecast model."

Most of the effort spent in that long evolutionary step has been to incorporate a relatively sophisticated surface and boundary layer scheme (Mailhot and Benoit 1982, hereinafter referred to as MB) and to complete the physics package with a formulation of the

Corresponding author address: Dr. Robert Benoit, DRPN, 5th Floor, West Isle Office Tower, 2121 Trans-Canada Service Rd. North, Dorval, Quebec H9P 1J3, Canada.

processes which we believed to be important for short-term forecasting (section 3).

During the inception and pursuit of this effort, we regarded the role of the physical processes in 48-hour regional forecasts as being dominated by the boundary layer and the surface fluxes (of heat, moisture and momentum). Although it was seen that the free atmosphere stratiform and convective condensations were the other key factors controlling short-term sources and sinks, we thought that these could be represented by simple formulations. In consequence, we regarded the matching of high-quality dynamics and boundary layer physics as important to simulate well weather elements such as low-level jets, fronts, heavy precipitation and intense cyclogenesis. To be consistent with the discretization of the driven model, the FE technique was adhered to from the very beginning of our boundary layer scheme. In order to discuss clearly how the various forcing terms are introduced, it is useful to review briefly the basic primitive equations (section 2). Since the success of a real-time operational model is the direct result of a delicate balance in a long sequence of operations, we present in section 4 the step-by-step operation of the RFE model. To illustrate the model performance, we give in section 5 results of the model forecast of the Presidents' Day Cyclone of 1979 and some statistics about the ongoing verification of model products and some computer system aspects. Of course, one learns by one's errors: some of our initial assumptions about model content is eventually put to question in section 6 and we indicate current research work on future versions of our regional model.

Due to its use in real-time NWP, the RFE is constantly subject to revisions and improvements; it is not a frozen model. We describe here a recently implemented version (October 1987).

2. The dynamical model

a. Governing equations

The starting point is the set of primitive equations as given by SD in their section 2. The moisture equation is written here in terms of specific density instead of dewpoint depression as in SD. The primitive equations describe the adiabatic motion of moist air provided we interpret the T symbol as being the virtual temperature $T_v = T[1 + (R_v/R_d - 1)q]$ and the R and R/c_p symbols as the dry air gas constant R_d and adiabatic constant $(R/c_p)_d$ respectively; R_v stands for the gas constant of water vapor and q its specific density. Note the change of definition for the symbol q which was used in SD for the logarithm of surface pressure. Pressure normalized by its surface value is used as vertical σ coordinate (see also section 2b).

To these equations, forcing terms are added to include the effects of physical processes on momentum, temperature and humidity. In other words, for $\psi = \mathbf{V}$, T or q, we consider the tendency ψ_t to be the sum of a dynamical (ψ_t^D) and a physical, or forcing (ψ_t^F), component: $\psi_t = \psi_t^D + \psi_t^F$. By referring to the definitions of ζ ($=\mathbf{k}\cdot\nabla\times\mathbf{V}$), D ($=\nabla\cdot\mathbf{V}$) and W_σ ($=-D$), we see that the proper form for the respective forcing terms are

$$\zeta_t^F = \mathbf{k}\cdot\nabla\times\mathbf{V}_t^F, \tag{2.1}$$

$$W_{\sigma\sigma t}^F = -D_{\sigma t}^F = -(\nabla\cdot\mathbf{V}_t^F)_\sigma. \tag{2.2}$$

These terms are added to the basic set to give

$$\zeta_t = G + \zeta_t^F, \tag{2.3}$$

$$\sigma W_{\sigma\sigma t} + R_d\nabla^2(T_v - \sigma T_{v\sigma}^* \log_e p_s) = \sigma(H - D_t^F)_\sigma, \tag{2.4}$$

$$T_{vt} - \sigma T_{v\sigma}^*(\log_e p_s)_t - \gamma_v^* W = J + T_{vt}^F, \tag{2.5}$$

$$(\log_e p_s)_t - W|_{\sigma=1} = -(\hat{\mathbf{V}})\cdot\nabla\log_e p_s, \tag{2.6}$$

$$q_t = -\mathbf{V}\cdot\nabla q - \dot{\sigma}q_\sigma + q_t^F. \tag{2.7}$$

The continuity equation (2.6) is unmodified since it is purely an expression of the conservation of air mass and no forcing of the mass is considered. All symbols not described above are as defined in Staniforth and Daley (1977).

The caret operator introduced to compute $\dot{\sigma}$ and W as integrals follows the modification of Béland and Beaudoin (1985) to properly include a lid at $\sigma = \sigma_1$ = the top of the vertical domain of the model. In order to control an instability due to the (semi-implicit) time scheme (Simmons et al. 1978), the reference profile is not taken to be the horizontal average of temperature but rather as

$$T_v^*(\sigma) = 320\ \text{K},$$

$$\gamma_v^*(\sigma) = \left(\frac{R}{c_p}\right)_d \frac{T_v^*}{\sigma}. \tag{2.8}$$

By the definition of T_v we have

$$T_{vt}^F = T_t^F[1 + (R_v/R_d - 1)q] + q_t^F(R_v/R_d - 1)T. \tag{2.9}$$

Here $\mathbf{V}_t^F$ includes horizontal diffusion ($\mathbf{V}_t^{F1}$) and vertical diffusion ($\mathbf{V}_t^{F2}$); T_t^F is made of horizontal diffusion (T_t^{F1}), vertical diffusion (T_t^{F2}), of heating by infrared radiation T_t^{FIR}, convection and condensation in the free atmosphere (T_t^{F3}); q_t^F has similar components except for radiation.

b. Discretization

The form of (2.3)–(2.7) has been especially selected to implement the semi-implicit time scheme with three time levels ($t - \Delta t$, t, $t + \Delta t$) denoted elsewhere by superscripts $n - 1$, n, $n + 1$. The current value of Δt is 10 minutes. A weak Robert time filter (Asselin 1972) is applied to control the $2\Delta t$ computational mode, viz,

$$\tilde{F}(t) = F(t) + \nu/2[F(t + \Delta t) - 2F(t) + \tilde{F}(t - \Delta t)], \quad \nu = 0.1.$$

Linear finite elements are used for discretization of functionals of the three space coordinates; the three-dimensional basis functions are chosen to be the triple product of the appropriate unidimensional chapeau functions $e^i(\omega)$:

$$e^i(\omega) = \begin{cases} \dfrac{\omega - \omega_{i-1}}{\omega_i - \omega_{i-1}}, & \text{for} \quad \omega_{i-1} \leqslant \omega \leqslant \omega_i \\ \dfrac{\omega_{i+1} - \omega}{\omega_{i+1} - \omega_i}, & \text{for} \quad \omega_i \leqslant \omega \leqslant \omega_{i+1} \\ 0, & \text{elsewhere,} \end{cases} \tag{2.10}$$

where ω is x, y or σ and $\{\omega_i,\ i = 1, N\}$ are the nodes along the corresponding axis; for the (half) boundary elements ($i = 1$ and N), one of the two segments of (2.10) is obviously discarded. Fields are expanded as

$$F(x, y, \sigma) = \sum_{i,j,k=1}^{N_i,N_j,N_k} F_{ijk}\theta^{ijk}(x, y, \sigma), \tag{2.11}$$

$$\theta^{ijk}(x, y, \sigma) = e^i(x)e^j(y)e^k(\sigma). \tag{2.12}$$

The term F_{ijk} represents the values of F at (x_i, y_j, σ_k) since $e^i(\omega_i) = 1$. The θ^{ijk} overlap only with their nearest neighbors, and the Galerkin procedure gives rise to sparse matrix problems and efficient algorithms.

Currently the horizontal resolution of the model over the central window (Δ) is 152.4 km. Figure 1 shows the full grid and a blowup of the central portion; all of the Northern Hemisphere is covered and the equator is tangent to the domain boundaries. The RFE model uses cartesian coordinates on a plane corresponding to the polar stereographic mapping of the globe, true at 60°N. The A-values shown on each of the four sides of the map are the amplification factors governing the grid stretching on the corresponding side, away from the central uniform window. The generation of the variable grid is explained in appendix A. In the present case, the central window has 56×39 points. It is seen that the stretchings are about 1.05 in every direction. Staniforth and Mitchell (1978) had noted the reduction in truncation errors when a smooth transition occurred between the central region and the outer mesh for a barotropic version of the model. This is found here to be even more crucial with the 3D version. Thus, a significant portion [$1 - (56 \times 39)/(101 \times 87) = 0.75$] of the computational points have to be put in the outer region. This is not excessive; for instance, Machenhauer and Haugen (1987) report the use of an extension zone outside the central region of the *barotropic* HIRLAM model that takes as much as 0.29 of the total number of points. One can then understand why, with our strategy and the *size* of the central region required in our application (i.e., at least all of Canada), it is difficult to achieve a very high resolution by the standards of regional modeling. We are also limited by the size of computer central memory because the FE technique almost requires that all full 3D grids be resident in core. Each 3D matrix at the current resolution takes 132 K words and 189 K words at $\Delta = 100$ km over the central window.

The choice of vertical resolution has been dictated mostly by the needs of the boundary layer formulation which is the solution of a time-dependent turbulent kinetic energy equation by the finite element technique. For this approach to succeed, a reasonable vertical resolution in the boundary layer is required, i.e., at least 3 or 4 levels in the first kilometer above the ground and ideally 3 or 4 times that so as to also resolve the thinner (~300 meter) nocturnal boundary layer; so far we have used a 15-level variable resolution vertical grid. In Fig. 2, the nodes start at the surface and have a geometric progression for their spacing (with a common ratio of 1.13) and reach $\sigma = 0.1$. The lowest spacing is 0.026, i.e., 220 m. In fact, the chosen type of distribution is identical to the "LEFT" subregion of each horizontal axis [cf. Eq. (A1a) of appendix A], with $R_1 = 1.13$, $M = 15$.

Note that in the calculation of some of the physical processes, the lowest level ($\sigma = 1$) is not considered to be at the ground interface itself but rather to have a thin surface layer below it, acting as a membrane controlling the vertical turbulent fluxes (more about this in section 3b). We shall call it the anemometer level.

c. *Solution of the dynamical equations*

As will be seen in the next section, the diabatic or forcing terms consist of diffusion operators, both along σ and in the horizontal, of adjustment terms (due to convection and condensation) and a source/sink term (due to terrestrial radiation). The horizontal diffusion is rather weak and is treated in a time-lagged manner. The vertical diffusion can be very strong in the boundary layer and it is solved with a fully implicit scheme. The last two types of terms are just considered as inhomogeneous tendencies.

As far as the dynamical aspects of the equations presented in section 2a are concerned, the treatment essentially follows the one of SD. Although a full time cycle of the RFE model involves four fractional steps (as in section 4d), we fix our attention here on the two major components:

Stage 1: all dynamical terms
Stage 2: all physical terms due to the boundary layer.

Stage 1 is solved with the semi-implicit time scheme and its time stability is governed by a CFL criterion due to advection. Assuming that stage 2 is dominated by the vertical diffusion, we now show how an implicit treatment of it does not restrict the overall time stability of the model.

Let ψ stand for V, T, or q. Following Bourke et al. (1977), we consider

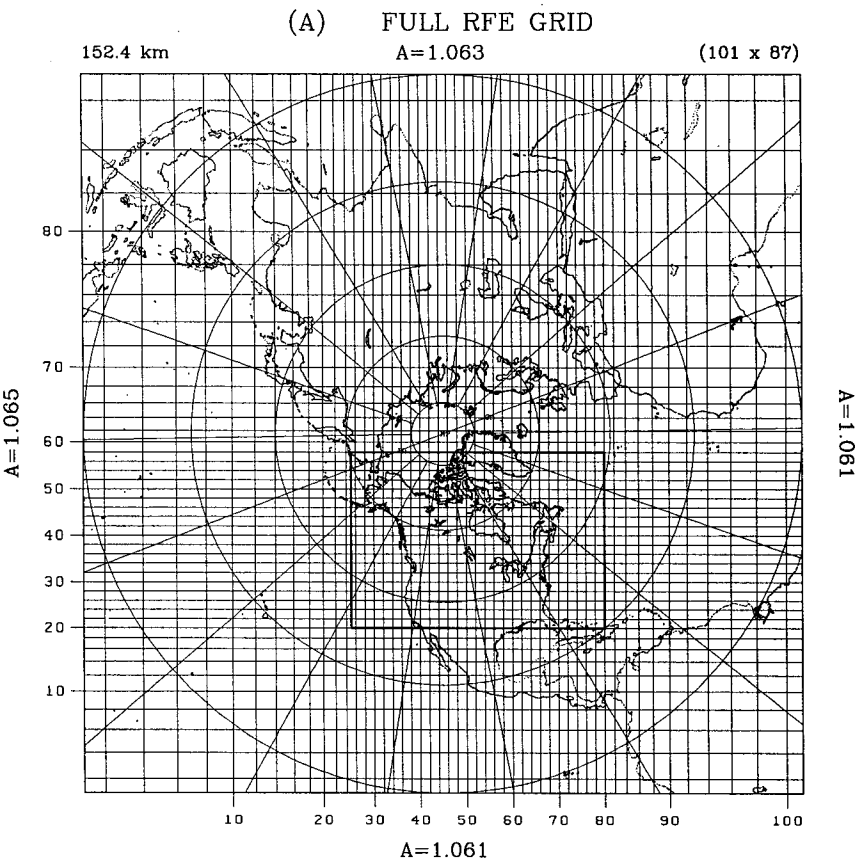

FIG. 1. (a) View of full RFE grid, including central portion with uniform resolution (152.4 km) window, outer variable resolution portion and lateral wall, tangent to equator. Only every *second* coordinate line is plotted. (b) Central portion of grid. A-values are stretching factors for each side of variable portion (outside intensified rectangle). Line numbering along graph edge is for the complete grid. Central region resolution is 152.4 km.

$$\psi_t + iK\psi = -N\psi \qquad (2.13)$$

as a prototype advective–diffusive equation ($N \geq 0$).

Our fractional step scheme applied to (2.13) is:

(Stage 1)

$$\frac{\psi^{*n+1} - \psi^{n-1}}{2\Delta t} = -iK\psi^n, \qquad (2.14)$$

(Stage 2)

$$\frac{\psi^{n+1} - \psi^{*n+1}}{2\Delta t} = -N\psi^{n+1}. \qquad (2.15)$$

The $*$ superscript indicates an interim variable, i.e., one which is not final in the sense that not all the processes have acted on it in the step from $n-1$ to $n+1$.

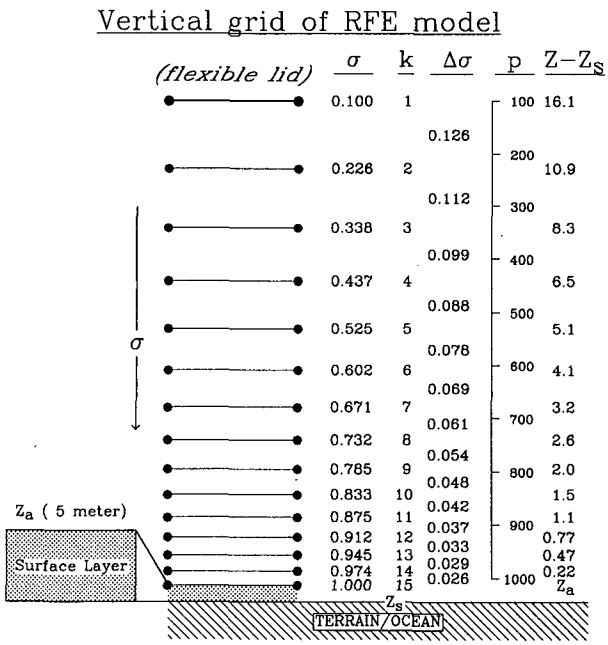

FIG. 2. Vertical distribution of levels for the model; σ is pressure normalized by the surface pressure. Levels are indexed (k) top down. Spacings ($\Delta\sigma$) are given, as well as nominal pressure (p, hPa) and elevation above terrain ($Z - Z_s$, km); the ICAO atmosphere was used. Fluid is confined by a flexible lid at top and by a thin (Z_a = 5 meter) turbulent surface layer near ground or ocean.

Equations (2.14)–(2.15) are solved for their complex amplification factor $X = \psi^{n+1}/\psi^n$:

$$X = \frac{-iK\Delta t \pm (1 + 2N\Delta t - (K\Delta t)^2)^{1/2}}{1 + 2N\Delta t}. \quad (2.16)$$

The existence of two roots is simply the manifestation of the well-known physical and computational modes arising in a three-time-level scheme.

In the absence of diffusion ($N = 0$), (2.16) reduces to $-iK\Delta t \pm (1 - (K\Delta t)^2)^{1/2}$. In the case of pure advection, we recover the CFL criterion $K\Delta t \leqslant 1$ for stability, and $|X| = 1$. If $N > 0$, then the radicand in (2.16) remains positive even for a certain range of $K\Delta t$ above 1; indeed, we obtain

$$|X| \leqslant 1 \quad \text{for} \quad K\Delta t \leqslant (1 + 2N\Delta t)^{1/2}, \quad (2.17)$$

which is thus the stable range of (2.14)–(2.15). The expression for the norm of the amplification factor is then

$$|X| = (1 + 2N\Delta t)^{-(1/2)}$$
$$= 1 - N\Delta t + \frac{3}{2}(N\Delta t)^2 + O(N\Delta t)^3, \quad (2.18)$$

compared with the analytical solution of (2.14):

$$|\exp - (iK + N)\Delta t| = \exp(-N\Delta t)$$
$$= 1 - N\Delta t + \frac{1}{2}(N\Delta t)^2 + O(N\Delta t)^3. \quad (2.19)$$

We see that our fractional scheme is of first-order accuracy in Δt for the diffusion term and its interaction with the advection term. Figure 3 displays the region of stability in the ($K\Delta t$, $N\Delta t$) plane, as well as the exact and numerical variations of $|X|$ with $N\Delta t$. Our analysis completely overlooks the variations of diffusivity (N) with σ and t; these are destabilizing factors which have been studied recently by Kalnay and Kanamitsu (1988) and whose findings are being incorporated in a future version of the RFE model.

3. Physical processes

Although the set of included processes is fairly comprehensive, we emphasize that most of the effort was put on those components deemed to be crucial for short range forecasting (i.e., diabatic boundary layer, items i–iv below, and free-atmosphere condensation/convection, items v and vi). The effects considered here are listed below, in approximately decreasing order of accuracy of the representation of the physical process.

(i) surface heat and moisture budgets;
(ii) stability-dependent surface layer exchanges;
(iii) turbulence and boundary layer diffusion;
(iv) surface characteristics (including topography);
(v) condensation;
(vi) free-atmosphere convection;
(vii) thermal and solar radiation;
(viii) cloudiness;
(ix) horizontal diffusion.

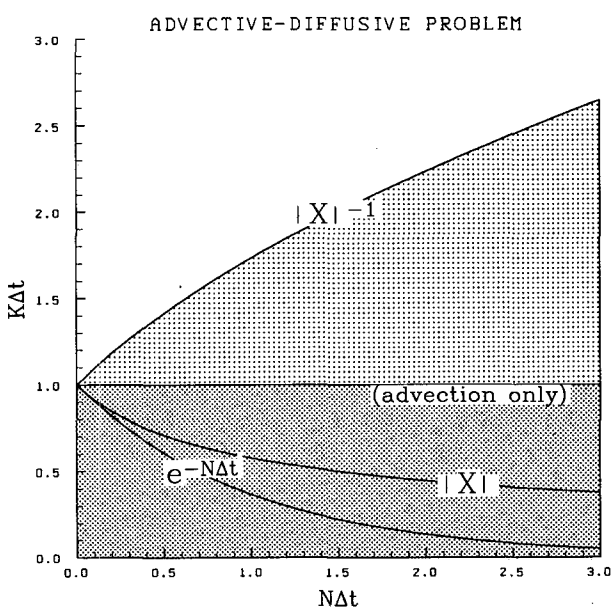

FIG. 3. Stability regions for the advective–diffusive problem of section 2c. $N\Delta t$ corresponds to a vertical diffusion CFL number and $K\Delta t$ is the advective CFL number. The module of the numerical amplification factor X is also plotted as well as its analytical value, $\exp(-N\Delta t)$. The denser stippling delineates the region of stability for pure advection ($N = 0$) while the lighter shade indicates the additional stable region when N is >0.

All these schemes are functions of time-dependent variables and interact, both mutually and with the dynamics of the RFE model, to produce acceleration/deceleration of the flow, heating/cooling and moistening/drying of the simulated atmosphere consistent with our knowledge of these processes. Radiation takes rank (vii) in our list because our treatment of it (cf. section 3g) was initially suited for a clear-air boundary layer model. Upon getting into the full RFE model, this was minimally upgraded by inclusion of simple cloud shadowing effects. This is causing cold biases in current forecasts and will be corrected in later versions.

For our purpose, we emphasize here the description of our schemes, especially the boundary layer and its relation to the other physical processes. The basic validation of the turbulence and surface scheme has been reported in MB; another paper (Mailhot and Chouinard 1989) investigates the sensitivity and impact of some components of our physics in the RFE model.

a. *Surface heat and moisture budgets*

The heat and water balances at the air–soil interface include solar and infrared fluxes, eddy exchanges of heat and vapor with the air, precipitation mass flux and heat and water diffusion into the soil. These balances are cast in the force–restore framework (Deardorff 1978) which models the surface (skin) temperature T_s and soil moisture fraction W_s (volume of water per unit volume of soil) as

$$\frac{\partial T_s}{\partial t} = \frac{-2\sqrt{\pi}}{C_s d_T}\left[H_s + L_v E_s + \epsilon_s(\sigma_{SB} T_s^4 - F_{Is}^-) - (1-\alpha_s)F_{Ss}^-\right] - \frac{2\pi}{\tau}(T_s - T_p), \quad (3.1)$$

$$\frac{\partial W_s}{\partial t} = \frac{-C_1}{\rho_w d_1}[E_s - R] - \frac{C_2}{\tau}(W_s - W_p), \qquad 0 \leqslant W_s \leqslant W_{\max}. \quad (3.2)$$

Here,

F_{Is}^-, F_{Ss}^-	incoming thermal and solar fluxes (cf. §3g);
ϵ_s, α_s, C_s	soil emissivity, albedo and heat capacity (cf. §3d);
τ	Earth rotation period;
d_T	depth of soil diffusion diurnal wave $= (\kappa_s \tau)^{1/2}$, κ_s being the soil thermal diffusivity;
T_p, W_p	deep soil temperature and moisture fraction;
H_s, E_s	turbulent fluxes of sensible heat and vapor (cf. §3b);
R	mass precipitation flux;
C_1, C_2	empirical moisture force–restore coefficients;
d_1	depth of skin moisture layer;
$W_{\max}$	run-off threshold;
ρ_w	water density;
σ_{SB}	Stefan–Boltzmann constant;
L_v	latent heat of vaporization.

The force–restore method is actually a closure condition on the heat and water balance at the air–soil interface. It assumes that unknown subsurface ground fluxes are carried out as diffusive processes; in that case, for a pure sinusoidal forcing (of diurnal period) at the interface, the surface value of the ground (heat) flux, G_s, can be shown to be

$$G_s = C_s d_T 2\sqrt{\pi}[\partial T_s/\partial t + 2\pi(T_s - T_p)/\tau]. \quad (3.3)$$

The coefficients $2\sqrt{\pi}$ and 2π are a consequence of the sine form for $G_s(t)$. It can be shown for a general periodic G_s, that the force–restore method responds exactly only to the fundamental harmonic, while the upper harmonics (T_s^n, $n \geqslant 2$) of T_s are reduced and phase-retarded according to

$$\frac{T_{s\,\text{F.R.}}^n}{T_{s\,\text{EXACT}}^n} = \left(\frac{2n}{1+n^2}\right)^{1/2} \exp\left[i\left(\frac{\pi}{4} - \tan^{-1} n\right)\right]; \quad (3.4)$$

for instance, the second harmonic ($n = 2$) is damped by $\sqrt{0.8}$ and delayed by about 0.05 period. The error due to the time discretization of the force–restore equation is not included here.

In the T_s equation (3.1), the ratio of the nondimensional coefficient of the restore term to the force term is $\sqrt{\pi}$ (≈ 1.77): this ratio applies to a purely diffusive process in the ground. For the moisture W_s, we shall see below (in section 3d) that C_1 is taken to be empirically dependent on W_s; the corresponding variation of C_2/C_1 can be explained as follows. In the moist soil limit, C_2/C_1 is 1.8 while for the dry soil case, C_2/C_1 tends to be $0.9/14 \approx 0.06$; this indicates that the water diffusivity is an increasing function of W_s and that the actual movement of W_s in the ground is significantly influenced by nondiffusive processes.

Here W_s is used as a moisture availability factor for the evaporation (Budyko-bucket method), which leads to our expression for air humidity at the surface

$$q_s - q_a = \min(1, W_s/W_k)(q_{SAT}(T_s) - q_a), \quad (3.5)$$

where W_k is a threshold for potential evaporation ($W_k < W_{\max}$) and q_a is the anemometer-level humidity. For the case of downward vapor flux, (3.5) erroneously has a dependence on soil moisture (i.e., W_s/W_k should be replaced by 1); fortunately, the flux value is generally small then. In contrast to the deep soil temperature, which is held constant during our short-term integrations of the model, we let W_p, the deep soil moisture vary according to

$$\frac{\partial W_p}{\partial t} = -\frac{1}{\rho_w d_2}[E_s - R],$$

where d_2 is chosen quite larger than d_1.

The computation of T_s and W_s is applied over all

grid points not considered as open sea (i.e., land points or ice-dominated ocean points). These time-dependent equations are handled with an implicit scheme using the time-step of the RFE model (currently 10 min). The weighting of times n and $n+1$ in the rhs of (3.1–3.2) is done according to $\alpha(\text{RHS})^{n+1} + (1-\alpha)(\text{RHS})^n$ with $\alpha = \frac{3}{4}$; this is considered as a compromise between optimal time truncation error ($\alpha = \frac{1}{2}$) and high-frequency damping ($\alpha = 1$). Thereafter a two-level time filter is applied:

$$\overline{\psi^{n+1}} = (1-\nu)\psi^{n+1} + \nu\bar{\psi}^n, \quad \psi = (T_s, W_s, W_p), \tag{3.6}$$

with $\nu = 0.1$.

Since those rhs contain nonlinear terms in T_s and W_s, a partial linearization is performed:

$$\text{RHS}'(T_s^{n+1}) = \frac{-2\sqrt{\pi}}{C_s d_T}\left\{K_1^n(T_s^{n+1} - T_a^n) + L_v K_2^n \frac{W_s^n}{W_k}\left[q_{\text{SAT}}^n + \frac{\partial q_{\text{SAT}}^n}{\partial T}(T_s^{n+1} - T_s^n) - q_a^n\right] + \epsilon_s \cdot \sigma_{\text{SB}}[T_s^{4n} + 4T_s^{3n}(T_s^{n+1} - T_s^n)]\right\}.$$

Only the nonlinear terms are shown above. The K_1, K_2 factors for the turbulent fluxes will be described in section 3b, and their complex variation with T_s^{n+1} is ignored in this linearization.

b. *Stability-dependent surface layer exchanges*

The surface layer is the first turbulent region occurring above the roughness elements where the vertical fluxes can be considered to be quasi-constant with height. This property gives rise to a simple (few parameters) structure in this (generally thin, ~10 m) layer. On the other hand, this is where the flow adjusts to the wall and very large shearing occurs; but we do not have to simulate this transition since this layer evolves in quasi-equilibrium, with an adjustment time scale much shorter than the RFE time-step, and the shear obeys a universal structure formula. No vegetative canopy is included.

The flexibility of the finite element technique allows us to put the last node at $\sigma = 1$, i.e., Earth's surface (in terms of pressure), but at the same time, for flux purposes, we assume that this is at a small height (Z_a) above the soil/water surface. For modeling purposes, we take Z_a to be generally 5 m, except over large roughness, where

$$Z_a = \max(5\text{ m}, 10Z_0); \tag{3.7}$$

in the context of our formulation, the ratio Z_a/Z_0 cannot get too close to 1. Thus, we consider the $\sigma = 1$ level as embedded in a surface layer and generally call it "anemometer level" (subscript a): i.e., θ_a stands for θ ($\sigma = 1$). As far as observations' standards are concerned, the real world's anemometer level is somewhat higher (around 10 m). For the modeling of surface exchanges, it is preferable to compute using a smaller value of Z_a in order to avoid turbulence intermittency in the stable case and to stay with simpler surface layer formulas.

Following MB the surface layer parameters are roughness length (Z_0) and static stability, expressed as a bulk Richardson number (Ri_B)

$$\text{Ri}_B = \frac{g}{\theta_{vs}} \frac{\theta_{va} - \theta_{vs}}{V_a^2 + w_*^2} \cdot Z_a, \tag{3.8}$$

where

θ_v virtual potential temperature $\left[= T(1 + 0.608q)\frac{\theta}{T}\right]$,

V module of physical velocity vector ($= |\mathbf{V}|$),

w_*^3 convective velocity scale (>0 only) $\left[= \frac{g}{\theta_{vs}}(\overline{w'\theta_v'})_s h\right]$,

h PBL height,

$(\overline{w'\theta_v'})_s$ flux of θ_v at the surface. (3.9)

The surface fluxes are computed from surface (i.e., subscript s) and $\sigma = 1$ quantities, according to

$$|\overline{w'V'}|_s = (C_M|V_a|)^2 \quad (= u_*^2, \text{ by definition}), \tag{3.10}$$

$$(\overline{w'\theta'})_s = C_M C_T |V_a|(\theta_s - \theta_a), \tag{3.11}$$

$$(\overline{w'q'})_s = C_M C_T |V_a|(q_s - q_a). \tag{3.12}$$

Here, C_M, C_T are functions of (Ri_B, Z_a/Z_0) (see Fig. 4); for instance, $1/C_M = \int_{Z_0}^{Z_a} \phi_M dZ/\kappa Z$, with ϕ_M the dimensionless wind gradient function and κ the von Kármán constant. Our formulation here is based on the flux-profile relationship given in (2.21)–(2.22) of MB, which ignores displacement height and implies a solution in term of Z/Z_0, where Z is distance to the surface. The dependance of C_M, C_T on roughness is mostly due to a $[\log_e(Z_a/Z_0)]^{-1}$ term; if Z_0 were greater or equal to Z_a, the transfer coefficients would become negative and thus nonphysical. This is the reason for the limitation of (3.7). Note that our expression for Ri_B is implicit since it includes a w_* term that itself depends on the heat-flux which we are trying to compute. The more conventional definition for Ri_B (Ri_B') is obtained from (3.8) by setting $w_* = 0$. The Ri_B' definition is used in Fig. 4. The lagged $(n-1)$ value of w_* is used to compute Ri_B^n. To obtain the so-called "internal stability parameter" (Z_a/L, where L is the Obukhov length) in the $\text{Ri}_B < 0$ case, we use an approximate relation

$$\log_e\left(\frac{Z_a}{L}\right) = \beta_L + \alpha_L \log_e(-\text{Ri}_B),$$

where β_L, α_L depend on Z_a/Z_0 and have been evaluated

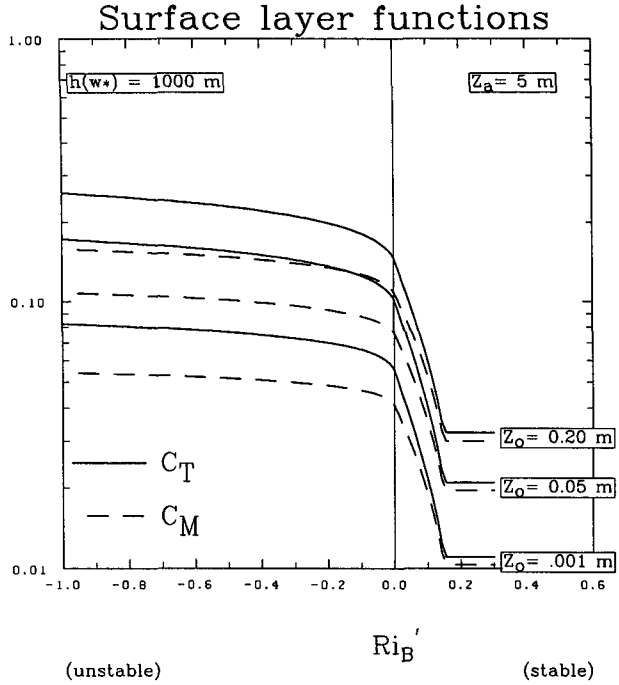

FIG. 4. The heat (C_T) and momentum (C_M) transfer coefficients as functions of $\mathrm{Ri}'_B = \frac{g}{\theta_{vs}} \frac{\theta_{va} - \theta_{vs}}{V_a^2} Z_a$, an external stability parameter. The computed functions include the effect of w_*^2 on Ri_B (cf. section 3b); for plotting purposes, w_* is calculated with h = 1000 m. Three sets of curves are shown: ocean, calm (Z_0 = 0.001 m); land, average (0.05) and rough (0.2). A rough ocean would have $Z_0 \approx 0.005$ m. See section 3d for a discussion on the magnitude of our Z_0 values.

in a least-squares fit of the above relation (with Ri_B replaced by Ri'_B):

$$\alpha_L = 0.98425 - 0.00514 \log_e \frac{Z_a}{Z_0} + 0.00021 \log_e^2 \frac{Z_a}{Z_0},$$

$$\beta_L = 0.40947 + 0.25344 \log_e \frac{Z_a}{Z_0} - 0.00580 \log_e^2 \frac{Z_a}{Z_0}.$$

As seen on Fig. 4, unstable conditions ($\mathrm{Ri}'_B < 0$) lead to enhanced transfer functions and vice versa for inversion conditions; when computing C_M and C_T in the latter case, Ri_B is kept smaller than its critical value ($\mathrm{Ri}_B \leq 0.7\ (\mathrm{Ri}_B)_{\mathrm{crit}} = 0.14$); in that way, C_M and C_T do not reach the zero limit, and small surface fluxes remain to take into account subgrid scale variations.

Surface layer theory and observations also provide most of the empirical parameters needed to close our turbulent diffusion scheme (see section 3c).

For the surface budget, the sensible heat and vapor fluxes are computed as

$$H_s = \rho_a c_p \left(\frac{T}{\theta}\right)_a (\overline{w'\theta'})_s,$$

$$E_s = \rho_a (\overline{w'q'})_s, \qquad (3.13)$$

where ρ_a is air density at the anemometer level.

c. *Turbulence and boundary layer diffusion*

The treatment of eddy vertical diffusion in the PBL rests on a time-dependent equation for the kinetic energy of turbulence (so-called TKE), E, which is the simplest and most basic of all higher moments often used to describe turbulent processes:

$$2E = \overline{u'u'} + \overline{v'v'} + \overline{w'w'}.$$

If E is known, then the diffusion coefficients for momentum (K_M) and heat/moisture (K_T) are expressed, following MB, as

$$K_M = a\sqrt{E}\lambda, \quad K_T = K_M/\mathrm{Pr}, \qquad (3.14)$$

where λ is a turbulent length scale (or a mixing length) and the Prandtl number Pr is by definition the ratio of the momentum and heat turbulent diffusivities; a is a nondimensional universal constant. Here λ is continuously tracking (with some relaxation time constant) either one of two equilibrium profiles, $\lambda_E[Z/h, \mathrm{sgn}(\mathrm{Ri}_B)]$ (see Fig. 5), following (2.15)–(2.17) of MB. The bulge on $\lambda_E(, -)$ allows for a maximum in K_M in the middle of the convective PBL.

After all closure is completed for E (see MB), the E equation is formally

$$\frac{dE}{dt} = \underbrace{BE^{1/2}}_{\text{(sources)}} - \underbrace{CE^{3/2}}_{\text{viscous dissipation}} + \underbrace{\frac{\partial}{\partial Z}\left(K_M \frac{\partial E}{\partial Z}\right)}_{\text{(redistribution)}}. \qquad (3.15)$$

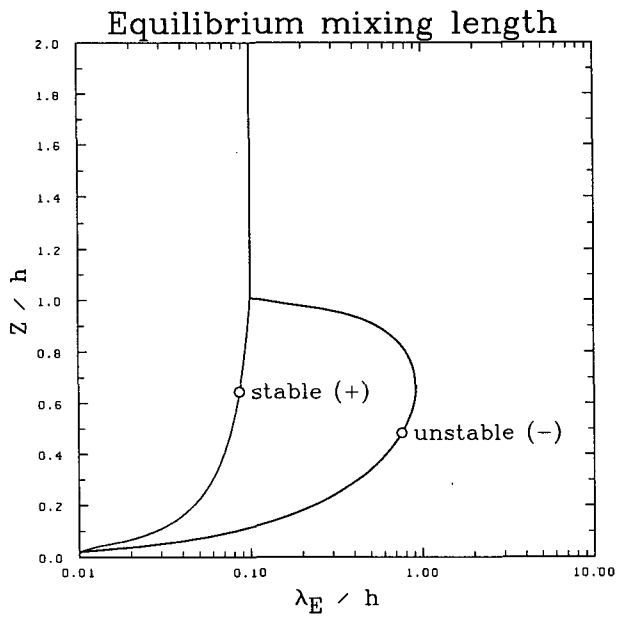

FIG. 5. The two branches of the parameterless function giving the equilibrium turbulent length scale λ_E in term of Z/h; λ_E (+) is used when the surface layer Ri_B is positive or zero (stable or neutral). Above $Z = h$, λ_E/h is set to 0.1, while near the surface, the two curves asymptote to $\kappa Z/h$.

Advection of E is currently neglected and the left-hand side reduces to $\partial E/\partial t$; the sources are production by shear and buoyancy and B can have either sign (amplification/decay of E) as expressed by the local Richardson number. The redistribution term can move eddy energy from a source to a sink region of the PBL (e.g., core of convective PBL to entrainment interface located at $Z = h$). In Eq. (3.15) C is positive and involves a dissipation length scale, taken as $\lambda_E(, +)$.

By time integrating Eqs. (2.15)–(2.16) of MB, the mixing length prognostic reduces to the solution of a transcendental equation in the unknown $\psi = \lambda^{n+1}/\lambda_E - 1$:

$$r_1 - \psi + \log \frac{r_1}{\psi} = r_2, \tag{3.16}$$

with

$$r_1 = \frac{\lambda^n}{\lambda_E} - 1,$$

$$r_2 = (|\overline{\mathbf{V}'w'}| + w_*^2)^{1/2} \Delta t \lambda_E^{-1}. \tag{3.17}$$

By using a combination of a generalized Newton–Raphson scheme (Bodewig's method) and of expansion by rational functions, machine accuracy is achieved with two iterations at most, throughout the parameter range ($-1 \leq r_1 < \infty$, $0 \leq r_2$).

The TKE equation is solved by a fractional step method:

$$\int_{n\Delta t}^{(n+1)\Delta t} dt = \int_{E^n}^{E^*} \frac{dE}{BE^{1/2} - CE^{3/2}}, \quad E \geq 0 \tag{3.18a}$$

$$\frac{E^{n+1} - E^*}{\Delta t} = \frac{\partial}{\partial Z}\left(K_m{}^n \frac{\partial E^{n+1}}{\partial Z}\right). \tag{3.18b}$$

The first part of the step (3.18a) is done exactly insofar as B and C can be assumed to be independent of time; the calculation is described in appendix B. The boundary conditions for (3.18b) are: no slope at the top level and E ($\sigma = 1$) $= E_a$ at the bottom level. Equation (3.18b) is followed by the application of the time filter [Eq. (3.6)] and of a vertical filter

$$\tilde{E}_k = E_k + \frac{\nu}{2}(E_{k+1} - 2E_k + E_{k-1}),$$

both with $\nu = 0.1$.

The Prandtl number Pr, the coefficient a of (3.14) and the lower boundary condition on the TKE are all taken from surface layer theory and assumed to hold (for the first two) across the whole PBL; see MB for more details. Figure 6 depicts the dependence on surface stability (and roughness).

We do not let $E = 0$ and a very weak background value is always enforced ($E_{\min} = 10^{-4}$ m^2 s^{-2}).

The thickness of the PBL is diagnosed from the vertical moments of the TKE density profile as

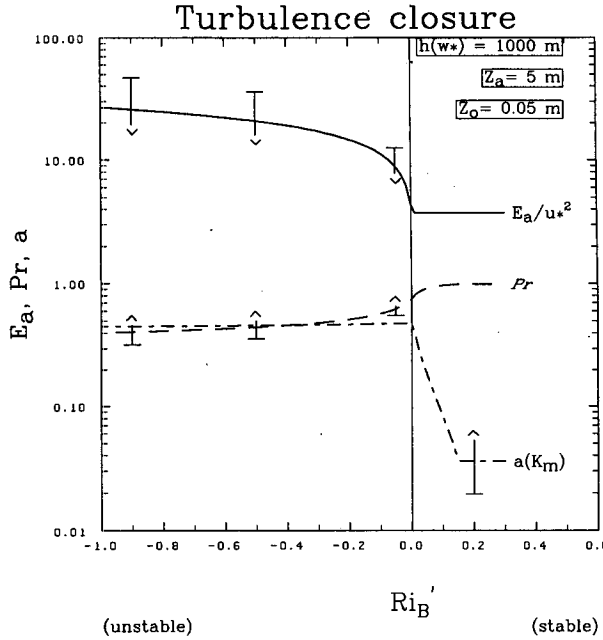

FIG. 6. Dependence of the three turbulence closure functions on surface layer stability (Ri'_B, external). The free-convection limitation (w_*^2) is computed here again with $h = 1000$ m. Some dependence on Z_0 exists for E_a and Pr on the unstable side and for a on the stable side. Bars (⊥) indicate sample variation as Z_0 changes from 0.001 to 0.20 m.

$$h = \bar{Z}^E + \mu[\overline{(Z - \bar{Z}^E)^2}^E]^{1/2}, \tag{3.19}$$

where

$$\overline{(\ )}^E = \frac{\int (\ )\rho E dZ}{\int \rho E dZ}. \tag{3.20}$$

The factor μ is set to 1.73 (0.21) for an unstable (stable) PBL; furthermore, only levels where E is sufficiently large, in the sense of

$$E \geq 0.01 E_a \text{ [}E_a \text{ from (2.25) of MB]},$$

$$E \geq 10 E_{\min},$$

are given nonzero weight in the above statistics. Also, h is not allowed to leave the range [300, 4000] meters.

Since our turbulence formulation is valid only for clear air (no condensation), we further prevent h from growing into a very moist layer (i.e., relative humidity in excess of 90%), at least when the PBL is unstable. If at any time the moisture in the first few layers exceeds that threshold, h is forced to its minimum value and, depending on the static stability (see sections 3e–f below), condensation may be allowed to act and remove the saturation condition.

All forcings due to surface and boundary layer turbulence on state variables are done as vertical diffusion operations (and a radiative diabatic term; see section 3g):

$$[\mathbf{V}, \theta, q]_t^{F2} = -\frac{1}{\rho}\frac{\partial}{\partial Z}\rho\overline{w'[\mathbf{V}', \theta', q']}, \quad (3.21)$$

$$\overline{w'\mathbf{V}'} = -K_M\frac{\partial}{\partial Z}\mathbf{V}, \quad (3.22)$$

$$\overline{w'q'} = -K_T\frac{\partial}{\partial Z}q, \quad (3.23)$$

$$\overline{w'\theta'} = -K_T\left(\frac{\partial}{\partial Z}\theta - \gamma_\theta H(k, k^+)\right). \quad (3.24)$$

The countergradient lapse rate γ_θ [see (2.7) of MB] is used to allow for concurrent upward heat flux and slightly positive θ lapse rate in the convective PBL. Here γ_θ is less than 2 K km^{-1} and is constrained to operate essentially below height h by a finite step function H which varies as 0.1, 0.5 and 0.9 as k changes, from $k^+ - 1$ to $k^+ + 1$, where k is the level index number (increasing downward) and k^+ is the first level above h (see the depiction of the levels in Fig. 8). Flux boundary conditions are used at both ends of the σ domain: insulated top (i.e., no fluxes) at σ_1; at $\sigma = 1$ (surface), continuity with surface-layer-governed fluxes. Details on the application of the FE technique are given in appendix C.

No additional free atmosphere vertical diffusion is included: we rely on the TKE equation to react to intermittently low values of the Richardson number and generate sufficient upper air turbulence to do the required mixing. An approximate lower bound for K_M in this scheme is

$$\min K_M \approx \min a \cdot \frac{h_{\min}}{10}\sqrt{E_{\min}} \approx 0.01 \text{ m}^2 \text{ s}^{-1}.$$

d. *Surface characteristics*

In order to perform calculations for the surface (section 3a) and surface layer (section 3b), many fields have to be specified:

1) land/sea mask ($M = 1/0$),
2) orography (Z_s),
3) surface roughness (Z_0),
4) albedo (α_s),
5) ice cover (G),
6) initial deep (W_p) and surface (W_s) soil moisture fractions.

Snow cover is not used directly by the RFE model at the moment (although it does affect our input albedo field).

Let us first consider the specification of the terrain (M), its height (Z_s), and its roughness (Z_0), which are interrelated and constitute the three most basic surface characteristics. For each of those, a low-latitude–low-resolution field reduction is invoked; it can be defined as

$$\psi' = w_1 w_2 \psi + (1 - w_1 w_2)\psi_{\text{low}},$$

$$w_1 = \begin{cases} 1, & \text{north of } 20°\text{N} \\ 0, & \text{south of } 15°\text{N}, \end{cases}$$

$$w_2 = \frac{(\Delta x^2 + \Delta y^2)_{\min}}{(\Delta x^2 + \Delta y^2)}, \quad (3.25)$$

for $\psi = Z_s$, M, Z_0; w_1 varies smoothly with latitude south of 20°N; w_2 depends on the ratio of local resolution to the resolution over the central region and is minimum near the outer wall; ψ_{low} is a limiting value. The limiting values are chosen to represent ocean surface characteristics: $Z_s = 0$, $M = 0$.

The terrain height data source is the so-called NCAR orography defined on an N36 global grid, reminiscent of an envelope orography. The land–sea mask data source is an N48 latitude–longitude grid. The RFE grid point value of M is taken as the value at the nearest neighbor on the N48 grid. The mask is adjusted to fit Z_s and to recognize the presence of the Great Lakes:

$$\begin{aligned} &\text{if} \quad M = 0 \quad \text{and} \quad Z_s > 25 \text{ m} \\ &\qquad \text{then} \quad M = 1 \quad \text{(outside of Lakes region)} \\ &\qquad\qquad\ \ M = 0 \quad \text{(Lakes region).} \end{aligned} \quad (3.26)$$

The initial roughness length field was provided by ECMWF, on an N48 grid, in which $Z_0 = Z_{0_{\min}} = 10^{-3}$ m over sea. This $Z_{0_{\min}}$ is used over sea only at initial time since later on, over the oceans, the roughness varies with time and space according to air flow (Charnock scheme) within observed bounds:

$$gZ_{0_{\text{sea}}} = 0.032u_*^2 \quad (1.5 \times 10^{-5} \leqslant Z_{0_{\text{sea}}} \leqslant 5 \times 10^{-3} \text{ m}).$$

Over land, the distribution is influenced by orography and vegetation (Louis 1984). Considering that the initial range goes up to about 10 m, a preliminary adjustment was needed to adapt it for use with our Z_a anemometer level, otherwise some of the transfer coefficients in the complete grid would be negative because of the $\log_e Z_a/Z_0$ behavior.

An empirical approach was taken to adjust the range of the Z_0 data to our low reference level (Z_a) such that C_M^2 behaves roughly like the drag field used in the early years of NWP (Cressman 1960).

The low-latitude–low-resolution reduction on the adjusted Z_0' is done on the quantity $C_M^2(Z_a/Z_0')$ which is more representative of the drag field. Here $C_{M\text{low}}^2$ is set to 1.4×10^{-3}. Finally, everywhere where $M = 0$, Z_0' is not allowed to get significantly above $Z_{0_{\min}}$.

Ice is merged into M according to $M + (1 - M)G$, and from then on no distinction is made between land points and ice-dominated sea points.

The final states of Z_s, Z_0, and M, as seen by the RFE forecasting program, are shown in Fig. 7, including the ice effect on M.

The albedo is analyzed on an N36 hemispheric grid, starting from an N48 monthly climatology and incor-

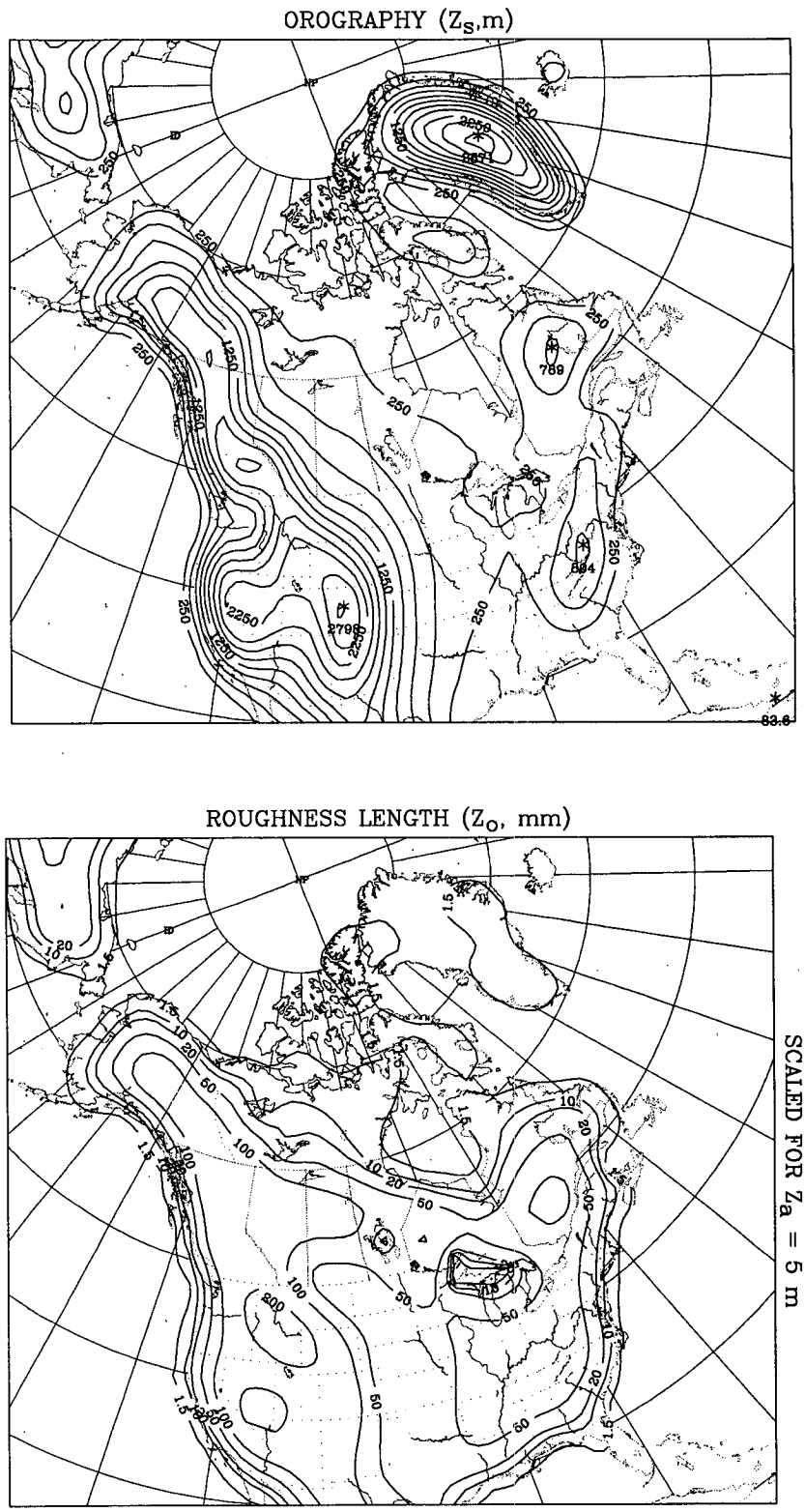

FIG. 7. The orography (a) and roughness length (b) as actually seen and used by the RFE time integration model. Contouring interval for Z_s is 250 m; for Z_0, the isolines are 1.5, 10, 20, 50, 100 and 200 mm.

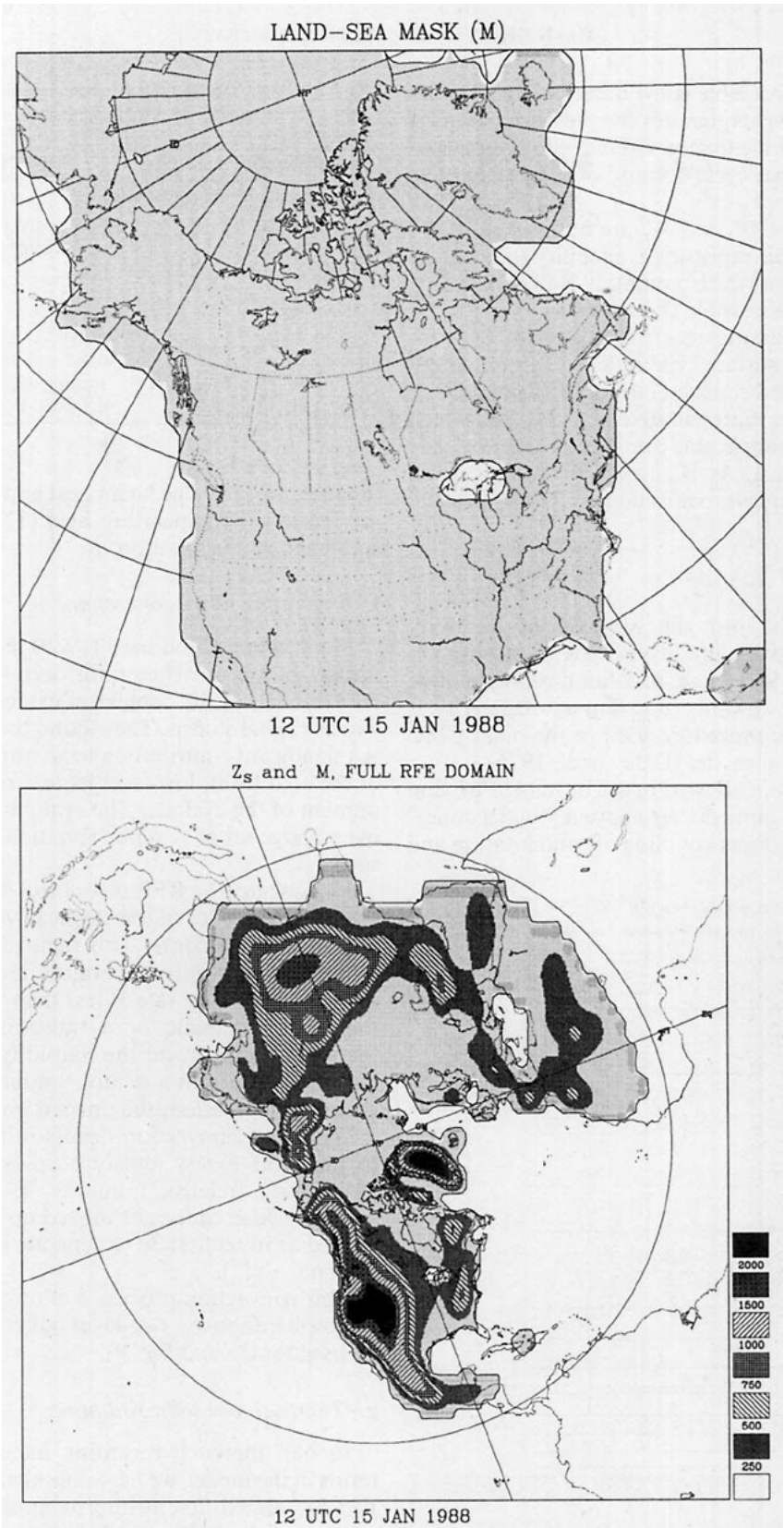

FIG. 7. (*Continued*) (c) is a sample of the land–sea mask for the winter season as actually seen and used by the RFE time integration model. The plotted isoline is $M = 0.9$ (1 = land or ice). The ice component is derived from climatology (and current analysis, if available). (d) shows Z_s and M on the full model domain. The first shading is for $M \geq 0.9$ and the higher ones are for orography. Note the transition to an ocean type of lower boundary in the low-latitude–low-resolution regions.

porating current available snow observations. The albedo analysis, however, ignores the presence of sea ice and thus these points, treated as land, can have a spuriously large diurnal cycle because of their rather low albedo.

Initial values for W_s and W_p are both taken as W_k times the input soil moisture availability (percentage of field capacity), for which a monthly N48 climatology from ECMWF is accessible (Louis 1984).

Other surface parameters are tabulated as functions of a single soil or surface type index. At the moment the index is assumed constant over all land points. The soil parameters are representative of a clay soil, which is considered to be applicable over North America; they are given in Table 1. As W_s evolves from dry to wet conditions, C_1 decreases continuously. The d_T thermal depth is 0.32 m.

TABLE 1. Values of the soil parameters used at each land point of the model. They correspond to a clay soil type.

Parameter	Value
ϵ_s	0.95
C_s	2.34×10^6 J m^{-3} K^{-1}
κ_s	1.20×10^{-6} m^2 s^{-1}
d_1	0.1 m
d_2	0.5 m
W_k	0.30
W_{max}	0.40
C_2	0.9
C_1	14 (dry; $W_s/W_{max} \leq 0.15$)
C_1	0.5 (wet; $W_s/W_{max} \geq 0.75$)

e. Condensation

Condensation is just the removal of humidity ($\rightarrow q_t^{F3}$) when relative humidity exceeds a condensation threshold (h_M = 90%) and a column-representative vertical motion is upwards ($\dot{\sigma} < 0$ at $\sigma = 0.7$). This is very similar to the procedure used in the older CMC operational spectral model (Daley et al. 1976).

This process is not allowed in the unstable PBL and the first two layers immediately above it ("buffer zone," Fig. 8), to prevent direct coupling of condensation and intense diffusion. The latent heat and moisture released are fed to the temperature field (T_t^{F3}) and to the instantaneous precipitation, R.

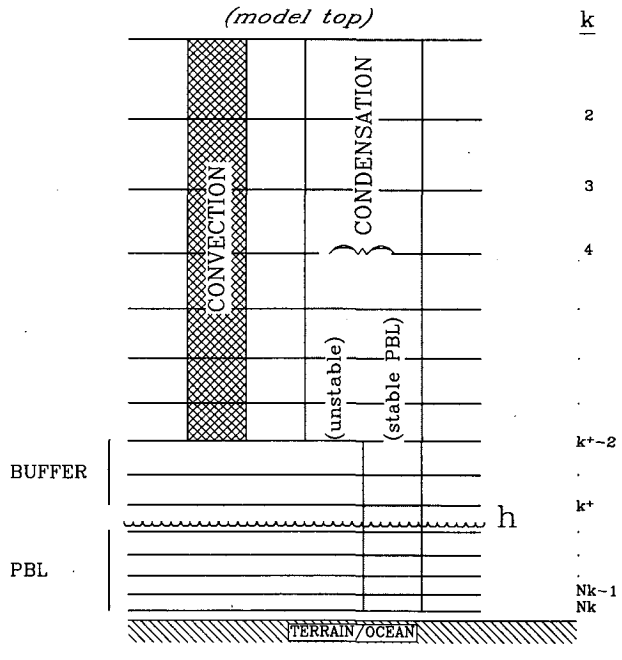

FIG. 8. The interfacing of convection and condensation processes with the boundary layer. Horizontal solid lines are model levels below h (wiggly line). The buffer zone is formed by the two adjacent σ layers starting at k^+, above h. The hatched regions indicate where each of the two processes is allowed to act. Note extension of condensation region when PBL is stable.

f. Free-atmosphere convection

Mailhot and Chouinard (1989) recently studied the impact of a Kuo scheme for deep convection in the RFE model, in the context of explosive deepening of winter coastal storms. They found that the Kuo scheme is a significant contribution to an improved simulation of the cold front, low-level jet and secondary redevelopment of the cyclone. The evaluation of this scheme over a large set of synoptic situations is currently pursued.

Meanwhile, the RFE model still uses a formulation (Daley et al. 1976) of the classical Manabe convective adjustment procedure. This removes static instability by mixing adjacent temperature levels ($\rightarrow T_t^{F3}$) such that the final lapse rate is less than the dry adiabatic, the moist adiabatic or a transitional combination thereof, dependent on the humidity of the layer (the transition begins at a relative humidity of h_c = 90%). As for condensation, the upward $\dot{\sigma}$ is also required.

Whenever convection occurs in that sense, we try to transport excess moisture upward to maintain a moist state (relative humidity $\geq h_F$ = 90%). The amount which cannot be moved up in this way is condensed as in section 3e to generate convective precipitation ($\rightarrow q_t^{F3}$).

This convection process is allowed only in the free atmosphere above a two-layer buffer zone and the PBL (see section 3e and Fig. 8).

g. Thermal and solar radiation

In our approach regarding inclusion of radiation terms in the model, we have considered that our physics package aimed first at improving the boundary layer portion of the RFE model, with lesser concern about the upper atmosphere at first. Consequently, we adopted the philosophy of Kondo (1971): for the boundary and surface layer, the infrared radiation divergence is of equal importance with the turbulence

mixing (upper PBL at night, surface layer during day), the solar absorption is negligible except at the surface itself, where it drives the diurnal cycle of the PBL.

No solar radiation absorption is computed on any σ level. We do only a solar flux calculation for the soil surface [cf. Eq. (3.1)]:

$$F_{Ss}^{-} = S_0 \cdot \tau_d \max(0, \cos\text{ZEN}) \cdot \tau_c, \quad (3.30)$$

where S_0 is the solar constant (1370 W m^{-2}), τ_d is an assumed clear air transmission factor of 65%, ZEN is the varying sun zenith angle, and τ_c is a reduction factor accounting for the presence of clouds (see section 3h).

Infrared cooling rates are computed at all levels from a scheme by Sasamori (1972). Only H_2O (rotational bands and 6.3 μm band) and CO_2 are considered to be active in the absorptivity; no cloud masking [but see (3.31), below] or liquid water effects are included. The scheme is done at every two hours of the model integration.

The surface flux, F_{Is}^{-} is computed independently of the cooling rates, following an empirical formula from Staley and Jurica (1972):

$$F_{Is}^{-} = 0.67\left[\frac{p_s q_a}{0.622}\right]^{0.08} B(Z_a) + \Delta F_{Is}^{-}. \quad (3.31)$$

The delta term is added to the original formula as a mean to enhance the flux in the presence of clouds (see section 3h).

h. Cloudiness

At the moment, clouds are computed only to get the cloud masking terms τ_c and ΔF_{Is}^{-} indicated in the previous subsection. Thus their only direct effect is on the ground surface [T_s equation, (3.1)].

The older ECMWF (before May 1985) cloud function is used (Geleyn 1980), whereby the cloud fraction C at any level is computed from the difference between relative humidity and a threshold function. Clouds are forbidden in the stratosphere ($\sigma < 0.225$) as well as in the boundary layer region ($\sigma > \sigma_{\text{PBL}}$), defined here as

$$\sigma_{\text{PBL}} = \begin{cases} 0.905, & \text{stable PBL} \\ \min(0.905, \sigma(h)), & \text{unstable PBL;} \end{cases}$$

here, $\sigma(h)$ is the σ value of the PBL height as given by Eq. (3.19).

To obtain the radiative correction terms, we follow a strategy used in the French operational models (Coiffier et al. 1986)

$$\tau_c = (1 - 0.4C_h)(1 - 0.7C_m)(1 - 0.7C_l) \quad (3.32)$$

$$\Delta F_{Is}^{-} = \sigma_{\text{SB}}[0.25T^4(\sigma_l)C_l + 0.27T^4(\sigma_m)C_m(1 - C_l) + 0.32T^4(\sigma_h)C_h(1 - C_m)(1 - C_l)]. \quad (3.33)$$

The high-, medium- and low-level cloud factors (C_h, C_m, C_l) are the maximum (overlap) values of C in each of three σ layers:

[0.225–0.395]: C_h

[0.395–0.710]: C_m

[0.710–σ_{PBL}]: C_l;

σ_h, σ_m, σ_l are the base levels for each of the three cloud groupings.

i. Horizontal diffusion

Horizontal diffusion is done very simply, by use of a linear ∇^2 operator, directly on σ surfaces. It is applied to relative vorticity (ζ), divergence (D), temperature (T) and specific humidity (q):

$$(\zeta, D, T, q)_t^{F1} = \nu\nabla^2(\zeta, D, T + \gamma_H Z_s, q). \quad (3.34)$$

All diffusivity coefficients here are taken as 10^5 m^2 s^{-1}. The $\gamma_H Z_s$ is a correction term to remove spurious heating over high terrain due to the natural pressure stratification of temperature (i.e., $T + \gamma_H Z_s$ is more constant than T is on a σ surface, $\gamma_H = 4$ K km^{-1}).

4. Operation of the model

We describe here the overall organization of the calculations done by the regional model starting from its data sources and ending with the preparation of a forecast.

The main steps are

1) horizontal interpolation to RFE grid and preliminary processing;
2) vertical interpolation to σ (terrain-following) coordinate;
3) initialization;
4) time integration.

a. Horizontal interpolation to RFE grid and preliminary processing

The interpolation scheme used here is a Lagrange polynomial in each direction (x, y), with the option of 0, 1, 2 or 3 for the degree; 0 actually means to take the interpolated value as the value at the nearest point on the input grid. The lower orders (<3) are used only for selected physics fields.

Fields interpolated from the hemispheric Gaussian grid of the analysis (180 × 45) to the RFE grid are: Φ, T, u, v, $T - T_d$ (p-levels).

In the interpolation of u, v, the velocity scalars ψ and χ are computed to account for the vorticity and divergence of the analyzed fields. The input gradients of $\nabla^2\psi$, $\nabla^2\chi$ are reduced gradually to zero starting at about 15°N and more as one approaches the square lateral wall situated near the equator. The aim is to eliminate the cross-boundary wind component and to establish a quiescent atmosphere next to the RFE lateral boundary.

Albedo is interpolated at zero order to the full RFE grid.

Finally, ice (G), T_s (both land and ocean portions) and T_p (deep soil temperature) are treated as three fields for which, in general, a real-time analysis (on some window) and a monthly background climatology (hemispheric or global) exist. Both sources are interpolated (zero order for ice, third order for the temperatures) either to the full RFE grid (background) or to the subset of the grid intersecting the analysis window (if available). The two interpolates are simply overlaid in a disjointed fashion. Over North America, T_s, T_p and G are analyzed on 190.5 km polar-stereographic windows. The ocean T_s analysis is on a coarse 381 km quasi-hemispheric window updated every six hours. We note in passing that the land T_s analysis is actually an air temperature analysis (Stevenson screen) and not the soil surface temperature, which in principle the model is treating with its force–restore scheme. The model rapidly adjusts T_s for this discrepancy.

b. *Vertical interpolation to σ (terrain) coordinate*

The interpolation scheme is cubic [in $\log_e(p)$] with slope and value specified at each data point; in the infrequent case where extrapolation is needed, first order is used at the top and second order below lowest (1000 hPa) pressure level. First, from humidity and temperature, the virtual temperature (T_v) is computed. Then, to get u, v, T_v and $T - T_d$ on σ levels, we compute slopes from finite differences except at the top p level where we use 0. The dewpoint spread $(T - T_d)(\sigma)$ is converted to specific humidity by making use of $T_v(\sigma)$.

c. *Initialization*

The success of the so-called nonlinear normal mode initialization technique (NMI) for the adjustment of initial time mass and flow fields towards a balanced state is well known for global or hemispheric models. It is more difficult, however, to apply this technique to a regional model because of nonseparability problems when spherical coordinates are not used (Verner and Benoit 1984). The operational RFE model now uses the implicit NMI (i.e., INMI) developed by Temperton (1988). The basis for that major breakthrough has been to notice that it is not essential to determine the normal modes explicitly in order to be able to carry out the balancing operation dictated by the NMI technique.

The INMI operates on time tendencies generated by the time integration program of the RFE (see section 4d) with all physical processes switched off. An elliptic differential equation is solved to obtain adjustments to the fields at each iteration. Three steps of nonlinear adjustments are taken. Only the four deeper vertical modes are balanced (equivalent depths greater than 100 m). To accommodate the rigid wall boundary at the edge of the RFE grid and the quiet corner regions, a low-latitude massaging is made, before the initialization, on the analysis south of 20°N, to achieve a zonally uniform state south of the equator. The divergent component of the analyzed wind is not removed from the σ fields before the INMI.

d. *Time integration*

The time discretization for the dynamics of the RFE model is semi-implicit and thus involves three time levels for leapfrogging; for the PBL physics and associated vertical diffusion, implicit schemes are used. The overall time scheme is a fractional step method with four stages: advection, horizontal diffusion, vertical diffusion, convection. Variables not having completed full sequences of the four stages will be termed "interim" and will be labeled as $\psi^{(k)}$ for the kth partial result.

At starting time, $t = 0$, and the operations described previously have provided $(u, v, T, q, W, p_s)^0$ as well as $(T_s, W_s, W_p, Z_0)^0$. Before going to $n = 1$, a few fields remain to be set:

$$R^0 = 0 \quad \text{(precipitation rate);}$$

$$h^0 = \frac{0.3u_*}{2\Omega \sin(\max(\phi, 20°\text{N}))} \quad \text{(Ekman formula for PBL height; } u_* \text{ calculated with } \mathrm{Ri}_B = 0\text{);}$$

$$\lambda^0 = \lambda_E(Z/h, -) \quad \text{(mixing length);}$$

$$E^0 = E_a \exp\left(-\frac{Z - Z_a}{h}\right) \quad \text{(turbulence).} \qquad (4.1)$$

The RFE time stepping is done by repeating the following operations (i) to (viii) for the required number of times (up to $t = 48$ h). No slow start is done at time zero, but rather a simple forward step takes place from $n = 0$ to $n = 1$.

(i) *Boundary layer/physics* block using as input:

$(\tilde{u}, \tilde{v}, \tilde{T}, \tilde{q}, \tilde{p}_s)^{n-1}$; R^n; $(E, \lambda, T_s, W_s, W_p, h, Z_0)^n$.

Do the schemes for surface, surface layer, radiation, clouds, and boundary layer turbulence. Compute vertical diffusion operators (K_M, Pr, γ_θ) and their boundary conditions for use in (v). The outputs are $(E, \lambda, T_s, W_s, W_p, h, Z_0)^{n+1}$.

(ii) *Dynamics* block. Using the three-dimensional FE technique, the primitive equations are solved with $(\mathbf{V}, T, q)_t^F = 0$, essentially as previously described in SD. Compute dynamical tendencies for vorticity, divergence, moisture and temperature, at time level n. Solve a three-dimensional Helmholtz equation for $W^{(1)}$, from which we compute a consistent $D^{(1)}$.

(iii) *Update.* Using all tendencies so far computed (without physics), obtain first interim values for time step $n + 1$, e.g.,

$$T^{(1)} - T^{n-1} = 2\Delta t \cdot (T_t^D)^n.$$

Output of (iii) is $(p_s, T, q, \zeta)^{(1)}$.

(iv) *Horizontal diffusion.* The contribution obtained from the application of the ∇^2 operator as described in

section 3i are used as $\psi^{(2)} - \psi^{(1)} = 2\Delta t \cdot (\psi_t^{F1})^{(1)}$. From the resulting $\zeta^{(2)}$ and $D^{(2)}$, we solve Poisson equations for the streamfunction and velocity potential subject to the lateral wall boundary condition, from which we recompute $(u, v)^{(2)}$.

(v) *Vertical diffusion.* Apply finite-element diffusion operators from (i) on u, v, $T(\theta)$, q to include all forcing terms due to vertical diffusion. The time scheme used for this operation is implicit and the combined advection–diffusion [i.e., (iii), (iv), (v)] problem is stable (cf. section 3b). This provides a third interim value for $n + 1$:

$$\psi^{(3)} - \psi^{(2)} = 2\Delta t \cdot (\psi_t^{F2})^{(3)}.$$

In the case of temperature, the radiative cooling term of section 3g is added on the right-hand side as an inhomogeneous term. In the case of momentum, the divergence is also adjusted, such that the relation between u, v and W is satisfied at the (3) level, i.e., $(W^{(3)} - W^{(2)})_\sigma = -\nabla \cdot (\mathbf{V}^{(3)} - \mathbf{V}^{(2)})$. In the case of moisture, we remove negative values: $q^{(3)} \geq 0$.

(vi) *Convection and condensation* on $T^{(3)}$, $q^{(3)}$:

$$(T, q)^{n+1} - (T, q)^{(3)} = 2\Delta t \cdot [(T, q)_t^{F3}]^{(3)}.$$

Generate rainfall rate, R^{n+1}, from q_t^{F3}.

(vii) *Time filter* on $(u, v, T, q, W, p_s)^n$ with coefficient $\nu = 0.1$. Enforce $q^n \geq 0$.

(viii) *End of time step.* $(\mathbf{V}, W, p_s)^{n+1} = (\mathbf{V}^{(3)}, W^{(3)}, p_s^{(1)})$.

5. A few model results

It is important at this point to present some details about performance. We shall do this by first looking at a well-known case as forecast here by the unmodified operational RFE model. We will finish this section by showing the main features of the objective performance scores and by giving some figures about computer system aspects.

a. Looking at a well-known case

Orlanski and Katzfey (1987, hereinafter referred to as OK) have recently used the case of the Presidents' Day cyclone of 18–19 February 1979 to study the sensitivity of model simulations relative to various options for the global nesting of a regional model. Our aim here is to illustrate the quality of forecast produced by an unmodified (i.e., the version described above) operational regional model relative to that achieved with a research-type model. Our results will be compared with those of the OK model running in simulation mode, i.e., with perfect analyzed fields in the outer region. In our case, only data from the initial time is used, and our resolution is quite coarser than OK's. The case is well described by Uccellini et al. (1985), and Atlas (1987) reviews previous forecasts made for this storm. The case has been studied recently again by Uccellini et al. (1987) who establish a synergistic relation between upper-level jet streaks and diabatic processes, particularly the PBL fluxes of sensible and latent heat, in the development of the coastal cyclone. Some of the previous simulations reviewed by Atlas (1987) also demonstrate a larger sensitivity to the surface fluxes.

We therefore consider this case to be a good candidate to measure the consistency (balance) or overall performance of an operational NWP system to perturbed synoptic conditions. As a consequence, the execution of a series of sensitivity runs to isolate the key factor is not justified here; the reader is referred to the study of Mailhot and Chouinard (1989) on the RFE physics/model. Our aim here is to show that the RFE forecast of the Presidents' Day Storm verifies well because it simulated properly both the upper air traveling

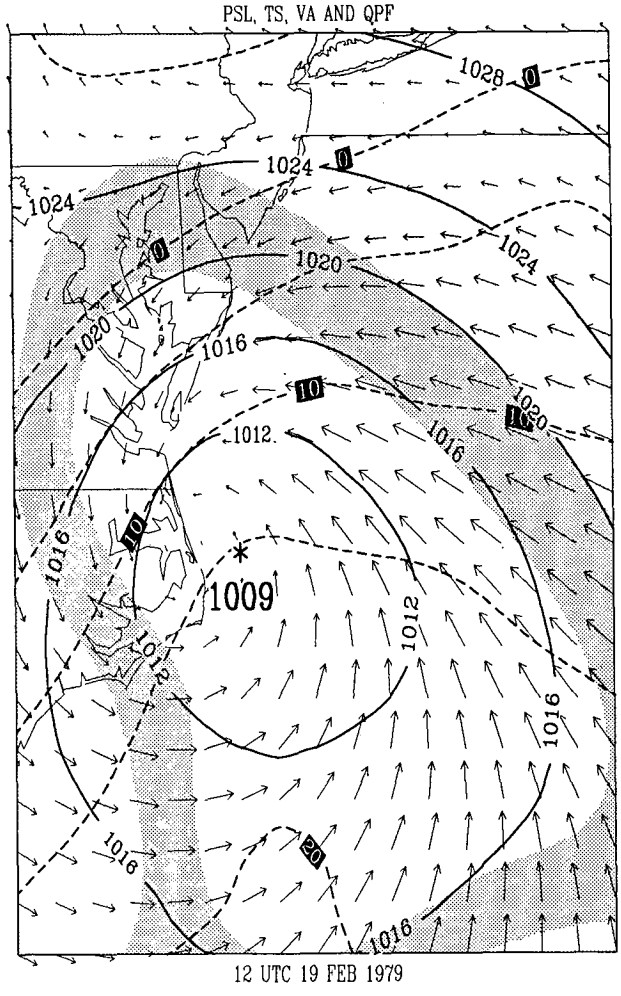

FIG. 9. Twenty-four hour forecast of sea level pressure (solid lines), anemometer level temperature (dashed) and wind (arrows, maximum speed = 19 m s^{-1}) and 6-h accumulated precipitation (mm) shading from 5 to 10, blank from 10 to 20). Same format as in Fig. 17 of Orlanski and Katzfey (1987).

intrusion and the coastal boundary layer and condensation.

We examine only the two main aspects, i.e., the explosive development of the low-level cyclone and the presence of the upper-level stratospheric fold and jet streak which were important to produce strong cyclogenesis. Just like OK, we start our model with the ECMWF version of the FGGE-3B analysis valid at 1200 UTC 18 February 1979. The model grid and parameters are as previously described in sections 2 to 4.

Figure 9 gives the RFE model 24 h forecast valid at 1200 UTC 19 February 1979; this is essentially in the

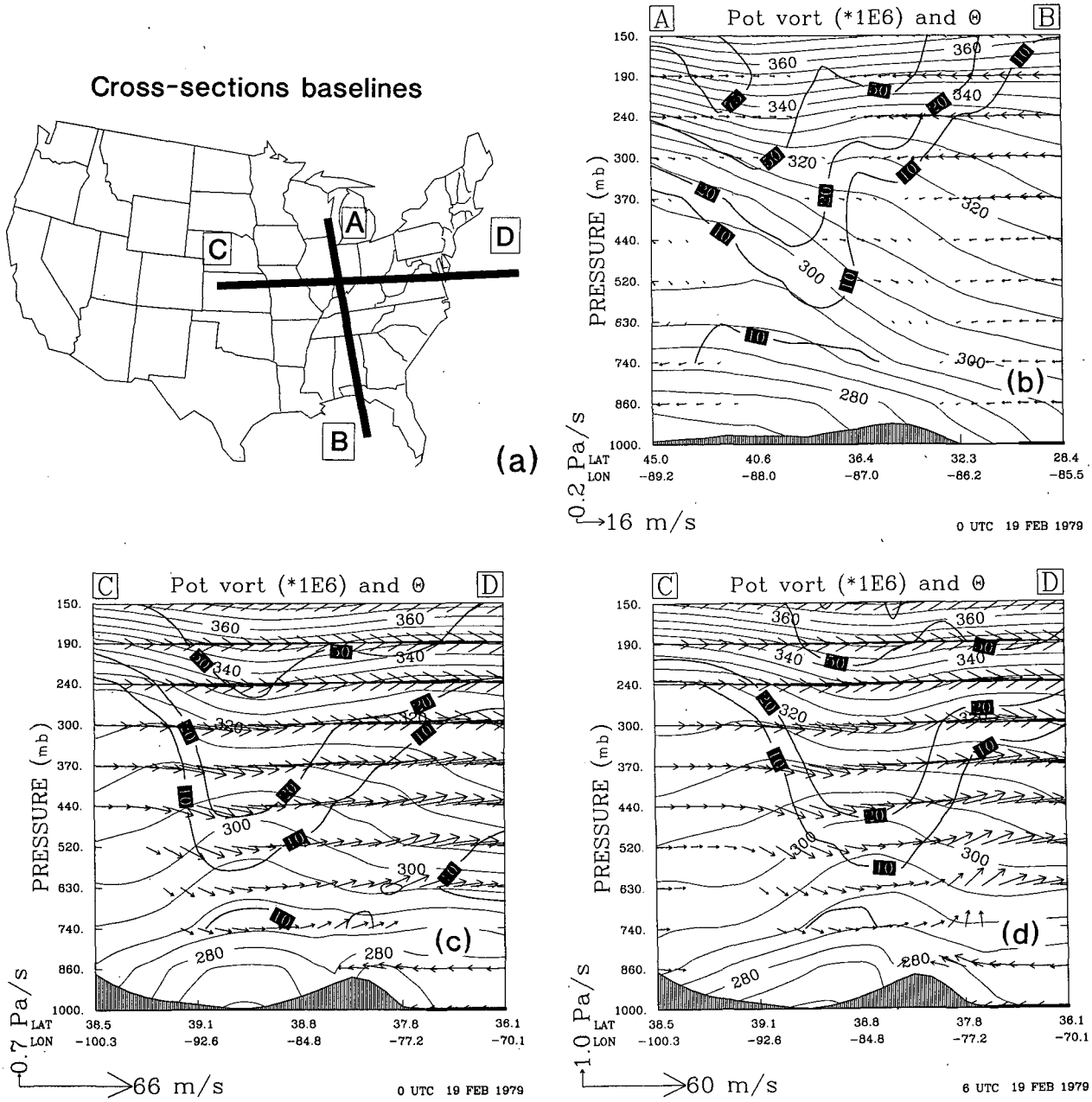

FIG. 10. Vertical cross-section of forecast fields from Green Bay, Wisconsin (A), to Apalachicola, Florida (B) for 0000 UTC 19 February 1979 [Panel (b)] and from Kansas (C) to offshore east of Delaware (D) [Panels (c)–(f)]. Panel (a) shows the two baselines. The heavy solid lines on the cross section are for potential vorticity (K mb^{-1} s^{-1}) scaled by 10^6; the thin lines are isentropes (K, interval of 5 K). The arrows depict the circulation in the plane of the cut; the vector scale is given in the lower left corner. The model orography (enhanced by 3 for A-B is shaded along the bottom of the cut; the position of model ocean area is also indicated there with a dark horizontal bar [e.g., over the Gulf of Mexico, in Panel (b)]. Format similar to Fig. 10b of Uccellini et al. (1985). A translation speed of 5 m s^{-1} to the right has been substracted from the wind.

same format as Fig. 17 of OK. The 5-m surface wind arrows are plotted every half degree (i.e., ≈50 km). Thus, the position of the minimum in sea level pressure agrees within one grid point with those of OK's model run in simulation mode (where the outer part of the domain is continuously set to analysis values) and of a mesoscale surface analysis by Bosart (1981) (also shown in that Fig. 17). With respect to Bosart's analysis, the RFE 150 km forecast has a pressure error of +4 hPa while OK's 50 km simulation has a −2 hPa error. The wind field is of comparable quality in the two models with a maximum speed of 19 m s^{-1} on our Fig. 9. The extent of the 6-h accumulated precipitation from the RFE agrees well with the land-based portion of Bosart's analysis: the entire Chesapeake and Delaware bays are covered by the 10 mm (and more) stippling while OK's model tends to hold the intense precipitation a bit too much toward the sea side. The weakest part of the RFE's forecast of the low is probably the anemometer level temperature with the 0°C isotherm displaced westward inland from the coast of New Jersey instead of remaining along the coastline as in Bosart's analysis. This is due in part to our use in this case of climatological surface parameter fields (albedo, surface temperature) since actual values are not provided with the FGGE analysis. The forecast thickness for the 500–1000 hPa layer at this time (not shown) positions the 540 dam line over Norfolk, in agreement with the FGGE analysis. The model QPF of Fig. 9 is thus expected to be snow, from Virginia to New York State. A 36-h integration ending at the same time gives similar results, with the central pressure slightly deeper, at 1007 hPa. Thus the prediction of the surface storm is well given by the RFE operational model in both integrations. All results shown, however, are from the 48 h run initiated on 1200 UTC 18 February 1979.

At the upper level, it is considered that the intrusion of stratospheric air and jet streak in the subtropical jet provided strong forcing for this surface cyclogenesis. This was emphasized particularly by Uccellini et al. (1985). Figures 10 and 11 in our paper are to be compared with their Figs. 10b and 4b. Descent of stratospheric air is identified by examining the potential vorticity $[-(\zeta + f)\partial\theta/\partial p]$ which is a quasi-conservative tracer. Figure 10b gives a cross section of the potential vorticity forecast with the isentropes and the vector circulation in the plane of the cut, running from Green Bay, Wisconsin to just south of Apalachicola, Florida (line labeled A-B on Fig. 10a). We see that the model stratosphere descends in a tongue shape down to about 600 hPa, (10×10^{-6} contour), above Nashville, Tennessee. The model's coarse resolution above 600 hPa has been sufficient to pick up this crucial dynamical feature.

We also ran a cross section west–east from Kansas to the Atlantic, at a position corresponding with the surface low at 1800 UTC (line labeled C-D on Fig. 10a); it is shown on Fig. 10c–f from 0000 UTC to 1800 UTC every six hours. At 0000 UTC, the stratospheric tongue hangs down to about 520 hPa, just west of the Mississippi, and with the vector field, it is possible to identify the three regimes of vertical motion shown in Fig. 7 of Uccellini et al. (1985): generalized subsidence for the whole column (up to 0.5 Pa s^{-1}) near 95°W; lower atmosphere ascent (up to −0.3 Pa s^{-1}) near 83°W, ahead of the polar jet trough; generalized ascent

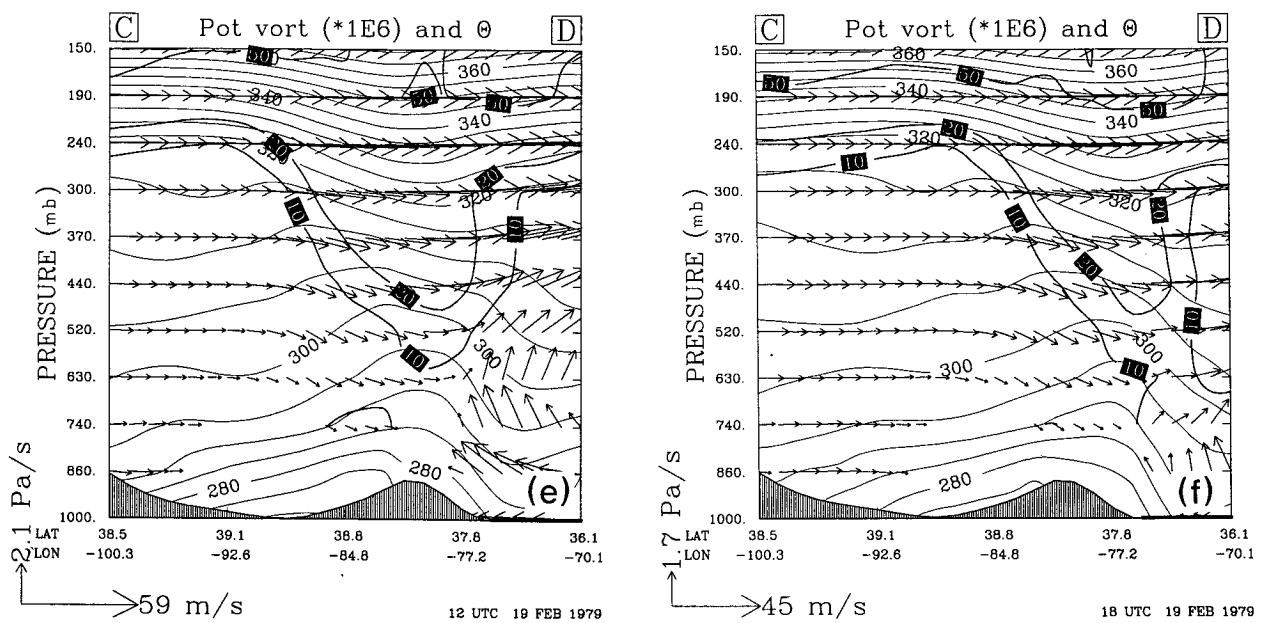

FIG. 10. (*Continued*)

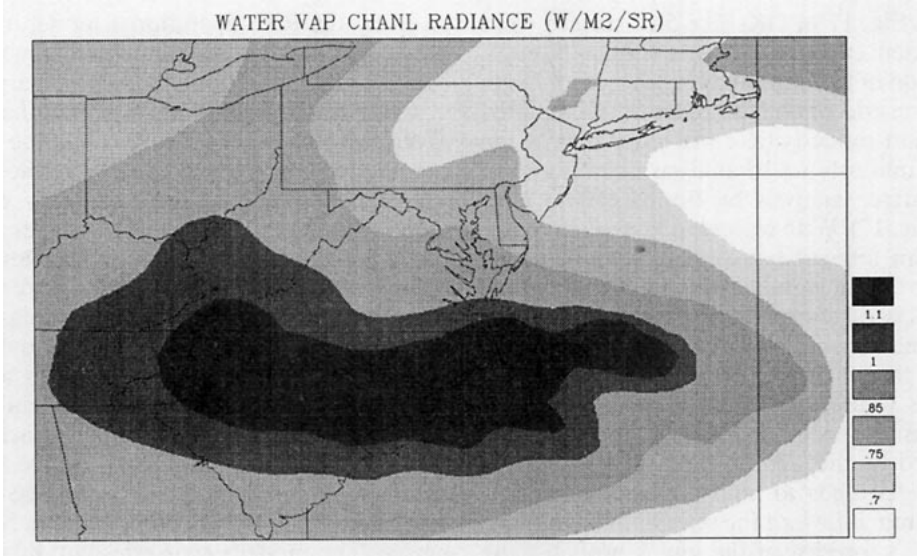

FIG. 11. Synthetic water-vapor channel (6.7 μm) radiance (W m^{-2} sr^{-1}) computed from model fields at 1800 UTC 19 February 1979. A 6-band spectral calculation was used. Grey scale shown on right. Same region and format as Fig. 4b of Uccellini et al. (1985): note error on shortened coastline in the latter figure, from Long Island to Boston.

(up to -5 Pa s^{-1}) for a column near the coast (77°W), in the subtropical jet. The remaining panels (Figs. 10d–f) illustrate the progression of the high-vorticity tongue eastward and downward. From 0600 UTC to 1200 UTC, it crosses the Appalachians and triggers a dramatic increase in the ascent above the deep (~800 hPa) oceanic mixed layer (potential temperature field). By 1800 UTC, the tongue has merged with the PBL vorticity. It is also possible to see that the layer of model air above freezing point on the sloping coastal plain of the Del–Mar–Va area is very shallow (less than 500 m); this again indicates solid phase precipitation.

Another aspect related to the stratospheric intrusion is the presence of a dry air slot. We finish by showing on Fig. 11 a synthetic water-vapor channel (6.7 μm) image computed from RFE model fields valid at 1800 UTC, on a window corresponding to Fig. 4b of Uccellini et al. (1985) which shows the corresponding Nimbus 7 satellite observation: details on the interpretation and significance of this infrared radiation channel are covered therein. The model forecast radiance agrees well with the observed one. The dark elongated blob shows the warmer flux upwelling from the lower air through the dry stratospheric tongue, and the lighter comma-shaped patch starting over New Jersey (bending over the ocean around the dark nose) is the reduced radiation from the upper level moist air over the cyclone itself.

b. *Objective performance scores*

Objective verifications are routinely computed by the Canadian Meteorological Centre (CMC) for NWP output from its two main models—the RFE (CDNRFE) and the 59-wave 19 levels hemispheric spectral (CDNSPE). Since the RFE emphasizes the PBL region, the improvements are expected therein; but it is difficult at the moment to extract useful RFE statistics from CMC's weather element verification package since it is still tailored to process data from the CDNSPE which was previously the earliest running main model here. So we fall back on the upper-air and gridded fields scores and then, as was found by the French Weather Service with their regional and hemispheric models, not much improvement is detected with these measures. The initial conditions and analysis system favor the CDNSPE since it runs from a more complete late analysis. We do not pretend here to present a comprehensive synoptic scale evaluation of our model such as the one done by Koch et al. (1985) for the MASS 52-km model of Kaplan et al. (1982) relative to the U.S. LFM 190-km model. The RFE is the first regional model implemented at the CMC and the verification programs are gradually adapted to monitor this newer type of operational model; for our purpose here we can only draw from somewhat shaky statistics. Nevertheless, Fig. 12 presents the main points.

Figure 12a shows the time evolution of the monthly mean temperature error at 850 hPa computed over the set of North American radiosondes: during more than half the lifetime of this version, the RFE has a cold bias of less than 0.5 K. For January/February 1988, however, the bias increases and the RFE loses its advantage over the CDNSPE. In terms of vector wind error, which is considered a good overall indicator, Fig. 12b shows that, at 850 hPa, the two models are on a similar footing, the RFE being slightly worse (particularly for the 1988 months): this is considered to be a

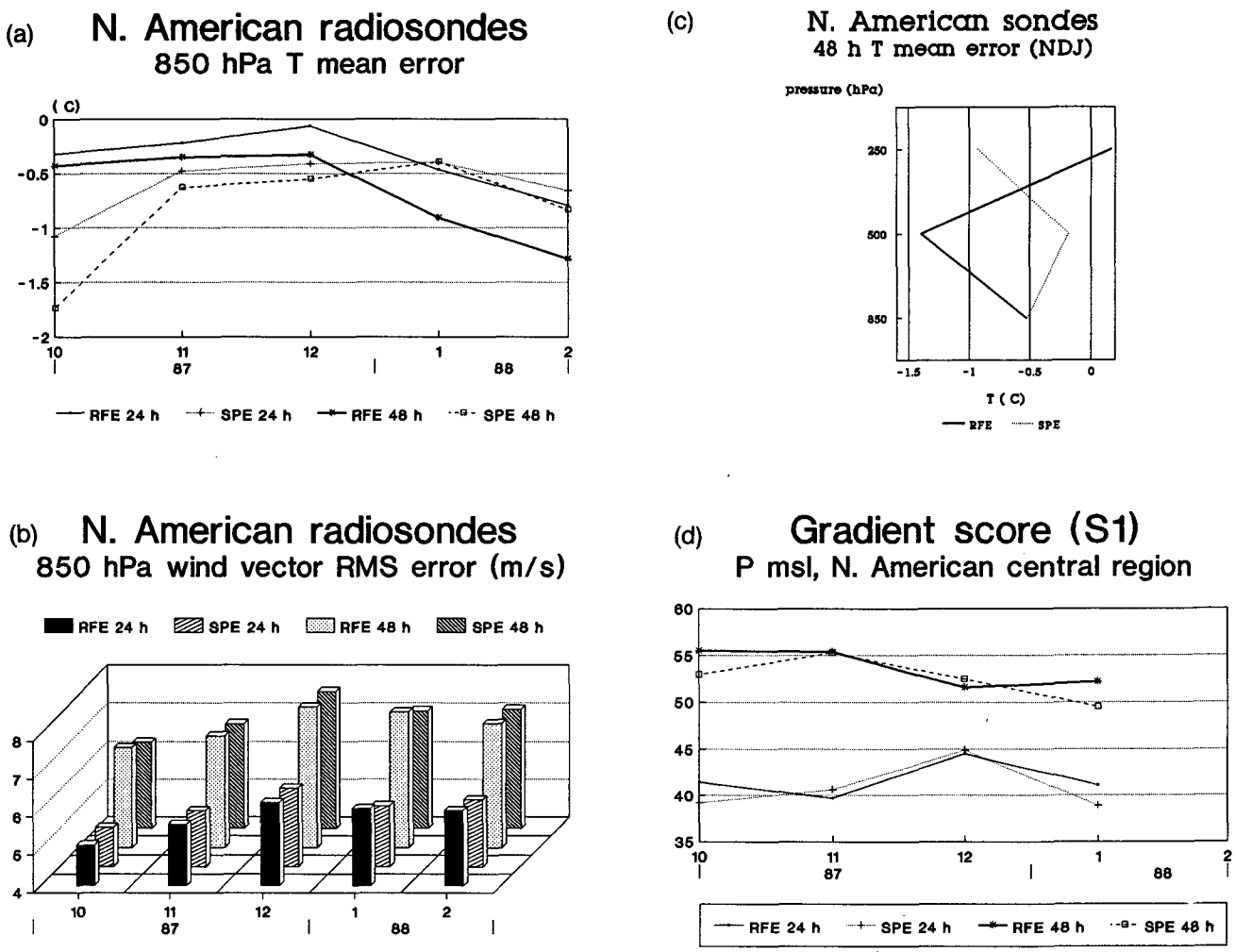

FIG. 12. Summary of objective performance scores for the RFE model, from October 1987 to February 1988. Panels (a)–(c) are derived from verification with the North American radiosondes network. The model is compared in all cases to the Canadian Spectral Model, running from late analysis to forecast up to 5 days. The 48-h mean temperature error profile of Panel (c) is an average for November 1987 to January 1988.

reflection of the RFE temperature bias. In consequence of the coarser resolution of the CDNRFE near the top, the rms wind error at 250 hPa is consistently larger, by about 0.6 m s^{-1}, than for the CDNSPE (approximately 11 and 15 m s^{-1} at 24 and 48 hours). The gradient score obtained by using the MSL pressure analysis (driven by the CDNSPE model) as the verifying field (Fig. 12d), again puts the two models on the same quality level; this is computed here over the central portion of North America (i.e., excluding the Rocky Mountains and the Appalachians, roughly). For various reasons, however, this S1 scoring could be biased and the radiosonde statistics are more reliable. Finally, we give in Fig. 12c what is probably, at the moment, the largest source of contamination acting in the RFE: the profile of 48-h mean temperature error over the radiosondes set highlights a marked cold bias of about −1.3°K in the midtroposphere for the CDNRFE. Recent sensitivity tests with the RFE show that this is mostly due to an imbalance in the heat sources profile caused by our simplified handling of radiation (particularly the complete absence of atmospheric solar absorption). Furthermore, the ongoing verification of the latest version of the RFE (with solar heating) running in parallel to the operational version also gives a much smaller 500 hPa cold bias. We also note that the CDNSPE has a full radiation scheme and exhibits essentially no midatmosphere temperature bias. The monthly mean 48-hour error maps for the RFE over America are about −2 hPa for sea level pressure and about −4 dam for 500 hPa height.

We close this subsection by showing a summary of pointwise verification statistics for 24-h accumulation of precipitation (Table 2) as obtained by interpolating the QPF grids to about 500 North American observing stations. The point forecasts and observations are then categorized along a 7-bin scale (0–0.2 mm up to 100–200 mm) and each verification is counted in a 7 × 7

TABLE 2. Pointwise verifications of 24-h precipitation forecasts for North American observing stations (north of 40°N).

Season	Model	PC (%)		PO (%)		PU (%)		*B* (no pcp) (%)	
	Forecast period (h)	24	48	24	48	24	48	24	48
(SON '87)	CDNSPE	68	57	18	32	15	10	92	69
	CDNRFE	70	63	11	20	19	17	109	97
(DJF '88)	CDNSPE	60	48	31	46	9	7	68	48
	CDNRFE	69	61	11	24	19	14	111	87
	Ideal	100		0		0		100	

Note. The scores in the above table are derived from a 7-category contingency table for precipitation quantities. Category 1 is for no precipitation (<0.2 mm), and category 7 is 100–200 mm. Let C_{ij} be an entry of the contingency table; the first index (i) is for the observation category, and the second one (j) is for the forecast category. The total number of cases (T) is $\sum_{ij} C_{ij}$. The parameters of Table 2 are then defined as follows.

$$\text{PC: percent correct} = \frac{\sum_i C_{ii}}{T};$$

$$\text{PO: percent overestimation} = \frac{\sum_{j>i} C_{ij}}{T};$$

$$\text{PU: percent underestimation} = \frac{\sum_{j<i} C_{ij}}{T};$$

$$B \text{ (no pcp): bias of category 1 (no precipitation)} = \frac{\sum_i C_{i1}}{\sum_j C_{1j}}.$$

$$\text{PC} + \text{PO} + \text{PU} = 1.$$

contingency matrix. About 12 000 pieces of data are thus verified over each 3-month season. The RFE 48-h percent correct (PC) values have an advantage of about 24 h over those of the SPE. Over the seven categories used, the overestimation (PO) is also much smaller for the RFE than for the SPE, but the RFE tends during those six months to underforecast the actual category (PU) a bit more than the SPE model. The advantage of the RFE QPFs shown by the over/underestimation statistics is also confirmed by considering separately the no-precipitation category and computing the ratio of the forecast frequency to the observed frequency [*B* (no pcp)]. Values above 1 indicate too rainy a forecast model and vice versa. The bias for the no-precipitation category [*B* (no pcp)] remains much closer to perfect (=100%) for the RFE model, with extremes of 87 and 111 (%). The QPF produced by the RFE, especially on Day 2, is considered to be the most reliable and useful of the two.

c. Computer system aspects

At present, the RFE model code uses very efficiently the CRAY XMP 28 machine of AES. It is essentially all vectorized (95⁺%), operating at an average rate of 130 MFlop on a single CPU. The model requires, for the operational grid selected, 2.5M 8-byte words (used in full dynamical allocation) and a 48-h forecast is prepared in 2500 seconds of CPU time. Due to the use of the fast access backing store (SSD, 7M words) for files, the input/output time is negligible. The output file is updated every 3 h and, by the end of the forecast, 32M pieces of weather information are available to the post-processors over North America and the neighboring oceans.

Multitasking and microtasking are being readied for the next version of the RFE, to optimize the use of the dual CPUs. In that way, it has been possible so far to dispatch to the two CPUs in parallel up to 92% of the single CP time, achieving a "best-case CPU to wall time" ratio of 1.8. Use of assembler-level code is very limited and a fully exportable version of the RFE is maintained on the library.

6. Summary and outlook

A description of the current parameterization of the physical processes as well as an overview of the complete Canadian regional finite element model has been given.

Sample results were presented in the form of a case study and some verification statistics. The operational RFE model, without any modification or tuning, gives a very good forecast of the Presidents' Day Cyclone of 1979; in particular, the distribution, intensity (and phase) of the heavy precipitation as well as the translation and role of the upstream stratospheric fold are

well simulated. The available large-scale performance statistics generally place the RFE on the same quality level as the Canadian Spectral model, with some advantages for the RFE with respect to QPF and low-level temperature. This version of the model, however, has a strong negative temperature bias in the midtroposphere.

To reduce the forecast errors and expand the set of forecast parameters, research versions of the RFE model have been run successfully with various upgraded features. Even prior to augmenting the formulations, our experience with the RFE indicates that it can benefit from enhanced resolution above 700 hPa, a deeper certification of the numerics for vertical diffusion and a close monitoring of its hydrological cycle (precipitation/condensation/evaporation). These versions are under evaluation for gradual implementation as the new operational RFE model within about two years. These studies deal with an improved boundary layer mixing length and turbulence transport, a Kuo package, split-phase precipitation, mesoscale resolution (~60 km) across Canada achieved with a two-time-level semi-Lagrangian advection scheme, a complete radiation scheme, the inclusion of shallow capping clouds in the PBL treatment, and a cloud water parameterization with tracer variables.

Acknowledgments. The authors give their thanks to Drs. Michel Béland and Andrew Staniforth for their lasting support during the many years taken by this work. During the last few years, Dr. Staniforth also headed with much talent the RFE model implementation team on the side of Division de Recherche en Prévision Numérique. On the side of the Centre Météorologique Canadien, the dedicated involvement of several meteorologists has and continues to be essential for the operational, real-time status of the RFE and its gradual improvement. The authors particularly thank Michel Roch, Angèle Simard and Gilles Verner for their role, and also Pierre Koclas and John Kurdyla. The expertise of Michel Valin for optimal use of the Cray computer is much recognized. They also appreciate the contribution of Réal D'Amours and Gary Toth for performance statistics. The manuscript was typed by Diane Lespérance, whose help is appreciated.

APPENDIX A

Generation of the Variable Grid

Since the generation of the nodes along the x and y axes is done similarly, we describe it only for the x axis. The boundaries are respectively at x_1 and x_N and three subregions are considered, each having a constant stretching. Let $h_i = x_{i+1} - x_i$, for $i = 1, \cdots, N-1$; each portion of the domain is then defined by:

LEFT ($1 \leqslant i \leqslant M$): M intervals, stretching $R_1 > 1$

$$h_i = R_1 h_{i+1} \tag{A1a}$$

CENTRAL ($M + 1 \leqslant i < M + L$): $L - 1$ intervals, stretching = 1

$$h_i = \Delta \tag{A1b}$$

RIGHT ($M + L + 1 \leqslant i < N$): $N - (M + L - 1)$ intervals, stretching $R_2 > 1$

$$h_i = R_2 h_{i-1}. \tag{A1c}$$

In each region, the spacings form a geometrical sequence,

$$h_i = R_1^{(M+1)-i}\Delta$$

$$h_i = \Delta$$

$$h_i = R_2^{i-(M+L-1)}\Delta, \tag{A2}$$

that can be summed to give the positions ($x_i - x_j = \sum_j^{i-1} h_k$):

$$x_{M+1} - x_1 = \frac{\Delta R_1}{R_1 - 1}(R_1^M - 1) \tag{A3a}$$

$$x_{M+L} - x_{M+1} = \Delta(L - 1) \tag{A3b}$$

$$x_N - x_{M+L} = \frac{\Delta R_2}{R_2 - 1}(R_2^{N-(M+L)} - 1). \tag{A3c}$$

The total length of the domain ($x_N - x_1 = \Lambda$), the central region spacing (Δ) and length (A3b) are given; R_1, R_2 and M are determined by solving an optimization problem:

"Minimize $(R_1 - R_2)^2$

subject to

$$\frac{R_1}{R_1 - 1}(R_1^M - 1) + \frac{R_2}{R_2 - 1}(R_2^{N-(M+L)} - 1) = \frac{\Lambda}{\Delta} - (L - 1)$$

$1 \leqslant M \leqslant N - (L + 1)$." (A4)

The equality constraint in (A4) results from the addition of the length components.

For the current operational grid of Fig. 1, N is 101, L is 56 and M, R_1, R_2 are found to be 24, 1.065, and 1.061, respectively. The resolution degradation incurred at a boundary point (h_1/Δ or h_{N-1}/Δ) is computed to be 4.53 (left, $=1.065^{24}$), 3.47 (right, $=1.061^{31}$), 3.08 (bottom, $=1.061^{19}$), 5.88 (top, $=1.063^{29}$).

APPENDIX B

Analytical Solution of the Source/Sink Part of $\partial E/\partial t$

We are solving here (3.18a):

$$\int_{n\Delta t}^{(n+1)\Delta t} dt = \int_{E^n}^{E^*} \frac{dE}{BE^{1/2} - CE^{3/2}}, \quad E \geqslant 0 \tag{3.18a}$$

with C positive definite and B real. The variable $\eta = \sqrt{E}$ is introduced, and $s = \pm 1 = \text{sgn}(B)$; the integrand may thus be rewritten as

$$\frac{2}{C}\frac{d\eta}{sD^2 - \eta^2} = dt, \tag{B1}$$

where $D^2 = |B|/C \geq 0$. The following cases fully describe the complete solution.

a. Case a

D^2 is zero. (B1) reduces to

$$\frac{-2}{C}\frac{d\eta}{\eta^2} = \frac{2}{C}d(\eta^{-1}) = dt, \tag{B2}$$

which yields

$$\eta^* = \left[(\eta^n)^{-1} + \frac{C\Delta t}{2}\right]^{-1}. \tag{B3}$$

b. Case b

$s = -1$. (B1) becomes

$$\frac{-2}{C}\frac{d\eta}{D^2 + \eta^2} = \frac{-2}{CD}d\left[\tan^{-1}\left(\frac{\eta}{D}\right)\right] = dt, \tag{B4}$$

which yields

$$\eta^* = D\tan\left\{\max\left[0, \tan^{-1}\left(\frac{\eta^n}{D}\right) - \frac{DC}{2}\Delta t\right]\right\}. \tag{B5}$$

η (or E) is decaying until it reaches zero and stays there afterwards since $dE/dt = 0$ for $E = 0$.

c. Case c

$s = +1$. (B1) becomes

$$\frac{2}{C}\frac{d\eta}{D^2 - \eta^2} = dt. \tag{B6}$$

We see that (B6) has a pole at $\eta = D$. This corresponds to an equilibrium value toward which η is asymptoting from its initial state η^n: $\lim_{\Delta t \to \infty} \eta^* = D$, in this case. There are three subcases for Case c.

1) CASE C1

$\eta^n < D$. η grows to D. (B6) yields

$$dt = \frac{2}{CD}d\left[\tanh^{-1}\left(\frac{\eta}{D}\right)\right]$$

and

$$\eta^* = D\tanh\left[\tanh^{-1}\left(\frac{\eta^n}{D}\right) + \frac{DC}{2}\Delta t\right]. \tag{B7}$$

2) CASE C2

$\eta^n = D$. The equilibrium is already achieved $\left(\frac{d\eta}{dt} = 0\right)$:

$$\eta^* = \eta^n. \tag{B8}$$

3) CASE C3

$\eta^n > D$. η reduces toward D. (B6) gives

$$dt = \frac{2}{CD}d\left[\coth^{-1}\left(\frac{\eta}{D}\right)\right] \tag{B9}$$

and

$$\eta^* = D\coth\left[\coth^{-1}\left(\frac{\eta^n}{D}\right) + \frac{DC}{2}\Delta t\right]. \tag{B10}$$

Finally, $E^* = (\eta^*)^2$. The time dependence of η^* is illustrated in Fig. 13 for all cases.

APPENDIX C

Solution of Vertical Diffusion Equation by the FE Technique

We want to solve our general vertical diffusion equation (3.21)–(3.24),

$$\psi_t = \frac{-1}{\rho}(\rho\overline{w'\psi'})_z$$

$$= \frac{1}{\rho}[\rho K_\psi(\psi_z - \gamma_\psi)]_z, \tag{C1}$$

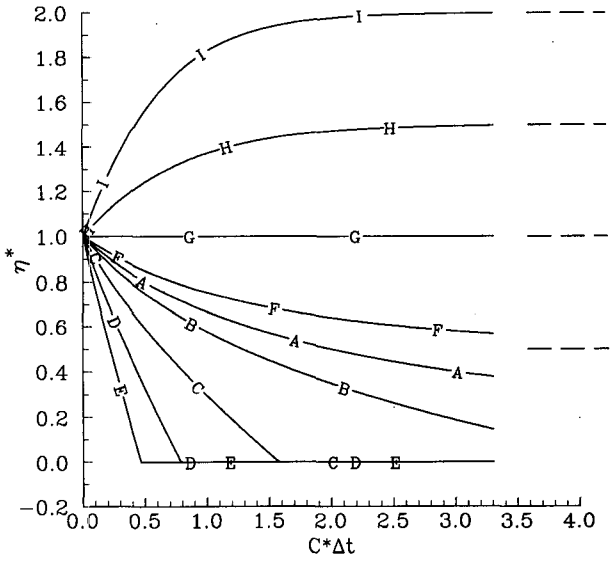

FIG. 13. Time variation of η^* in the solution of the sources/sinks terms of $\partial E/\partial t$; η^n is chosen to be 1. Curves are labeled A through I. A = case a. B-C-D-E = case b, with D = ½, 1, 3/2, 2. F = case c1; G = case c2; H-I = case c3. Same values of D used in F–I as in B–E. Asymptotes for F-I curves are marked by dashed lines on the right.

for $\psi = u, v, \theta, q$ or E. At the top of the domain, a no-flux condition is imposed

$$K_\psi(\psi_Z - \gamma_\psi)|_{\text{top}} = 0, \tag{C2}$$

while at the base of the domain, taken to be the anemometer level, the condition is continuity of flux for $\psi \neq E$

$$K_\psi(\psi_Z - \gamma_\psi)|_a = C_\psi C_M V_a(\psi_a - \psi_s), \tag{C3}$$

and an imposed surface layer expression for $\psi = E$, i.e., $\psi = E_a$.

Before proceeding, (C1)–(C3) are transformed for the sigma coordinate:

$$\psi_t = [\tilde{K}_\psi(\psi_\sigma + \tilde{\gamma}_\psi)]_\sigma; \tag{C4}$$

$$\tilde{K}_\psi(\psi_\sigma + \tilde{\gamma}_\psi)|_{\sigma_1} = 0; \tag{C5}$$

$$\tilde{K}_\psi(\psi_\sigma + \tilde{\gamma}_\psi)|_{\sigma=1} = -AC_\psi C_M V_a(\psi_a - \psi_s); \tag{C6}$$

$$A = \frac{g\sigma}{RT}; \tag{C7}$$

$$\tilde{K}_\psi = A^2 K_\psi; \tag{C8}$$

$$\tilde{\gamma}_\psi = A^{-1}\gamma_\psi. \tag{C9}$$

The time discretization is implicit, with the time step $\Delta t'$, being either $2\Delta t$ for $\psi \neq E$ or Δt, for $\psi = E$. The initial value (at time $n-1$ or n) is denoted by ψ^*:

$$\frac{\psi^{n+1} - \psi^*}{\Delta t'} = [\tilde{K}_\psi^*(\psi_\sigma{}^{n+1} + \tilde{\gamma}_\psi)]_\sigma, \tag{C10}$$

subject to

$$\tilde{K}_\psi^*(\psi_\sigma{}^{n+1} + \tilde{\gamma}_\psi)|_{\sigma_1} = 0; \tag{C11}$$

$$(\psi \neq E): \quad \tilde{K}_\psi^*(\psi_\sigma{}^{n+1} + \tilde{\gamma}_\psi)|_{\sigma=1} = -A(C_\psi C_M V_a)^{n-1}(\psi^{n+1} - \psi_s{}^{n+1}); \tag{C12}$$

$$(\psi = E): \quad \psi^{n+1}|_{\sigma=1} = E_a{}^n. \tag{C13}$$

For $\psi = E$, $\tilde{K}_\psi^*$ is computed from E^n [and not E^*; cf. (3.18)], while for $\psi \neq E$, $\tilde{K}_\psi^*$ is computed from E^{n+1}.

The σ discretization is an application of the FE technique similar to MB (their section 3d and Appendix). After orthogonalizing the space discretization error of (C10) to the basis, one obtains

$$\int_{\sigma_1}^1 e^k \Delta\psi d\sigma = e^k J|_{\sigma_1}^1 - \int_{\sigma_1}^1 e_\sigma{}^k J d\sigma, \tag{C14}$$

where

$$\Delta\psi = \psi^{n+1} - \psi^*, \tag{C15}$$

$$J = \Delta t' \tilde{K}_\psi^*(\psi_\sigma{}^{n+1} + \tilde{\gamma}_\psi). \tag{C16}$$

Boundary conditions (C11)–(C12) are substituted for the first term on the rhs of (C14). In the case of $\psi = E$, (C13) gives us $\Delta\psi|_{\sigma=1} = \Delta\psi_N$ and the equation is solved only on the reduced set of levels $\sigma_1 \ldots \sigma_{N-1}$, where the boundary term of the rhs is completely absent. Otherwise, for $\psi \neq E$, letting $B = -A(C_\psi C_M V_a)^{n-1}\Delta t'$, the boundary term becomes

$$e^k J|_{\sigma_1}^1 = e^k(\sigma = 1)B(\psi_N{}^{n+1} - \psi_s{}^{n+1}) = \delta_{kN}B[\Delta\psi_N - (\psi_s{}^{n+1} - \psi_N^*)]. \tag{C17}$$

Expanding the dependent variables $\Delta\psi$, ψ^*, $\tilde{K}_\psi^*$ and $\tilde{\gamma}_\psi$ on the vertical FE basis as in (2.11), one arrives at the matrix problem

$$(\mathbf{P} + \mathbf{D}_K - \mathbf{B})\Delta\psi = -\mathbf{D}_K\psi^* - \mathbf{M}_K\gamma_\psi - \mathbf{B}(\psi_s{}^{n+1} - \psi^*), \tag{C18}$$

with

$$\mathbf{P} = \int_{\sigma_1}^1 e^i e^k d\sigma;$$

$$\mathbf{D}_k = \Delta t' \int_{\sigma_1}^1 \tilde{K}_\psi^* e^j e_\sigma{}^i e_\sigma{}^k d\sigma;$$

$$\mathbf{M}_k = \Delta t' \int_{\sigma_1}^1 \tilde{K}_\psi^* e^j e^i e_\sigma{}^k d\sigma;$$

$$\mathbf{B} = \delta_{iN}\delta_{kN}B. \tag{C19}$$

Equation (C18) is solved for $\Delta\psi$. Sums over repeated index are implied in the above. We note that the discrete equations (C18) ($k = 1, N$) conserve the net boundary flux, as does the continuous form [(C10) or (C4)]:

$$\frac{\partial}{\partial t}\int_{\sigma_1}^1 \psi d\sigma = \tilde{K}_\psi(\psi_\sigma + \tilde{\gamma}_\psi)|_{\sigma_1}^1; \tag{C20}$$

by summing all lines of the (C18) system ($\sum_k$) and using the property that $\sum_{k=1}^N e^k(\sigma) = 1$, the following relation is deduced:

$$\int_{\sigma_1}^1 \Delta\psi d\sigma - B\Delta\psi_N = -B(\psi_s{}^{n+1} - \psi_N^*);$$

i.e.,

$$\int_{\sigma_1}^1 \Delta\psi d\sigma = B(\psi_N{}^{n+1} - \psi_s{}^{n+1}). \tag{C21}$$

This last expression is identical with the exact result (C20), up to time truncation errors.

REFERENCES

Anthes, R. A., 1983: Regional models of the atmosphere in middle latitudes. *Mon. Wea. Rev.*, **111**, 1306–1335.

Asselin, R., 1972: Frequency filter for time integrations. *Mon. Wea. Rev.*, **100**, 487–490.

Atlas, R., 1987: The role of oceanic fluxes and initial data in the numerical prediction of an intense coastal storm. *Dyn. Atmos. Oceans*, **10**, 359–388.

Béland, M., and C. Beaudoin, 1985: A global spectral model with a

finite element formulation for the vertical discretization: adiabatic formulation. *Mon. Wea. Rev.*, **113,** 1910–1919.

Bosart, L. F., 1981: The Presidents' Day snowstorm of 18–19 February 1979: A subsynoptic-scale event. *Mon. Wea. Rev.*, **109,** 1542–1566.

Bourke, W., B. McAvaney, K. Puri and R. Thurling, 1977: Spectral methods for atmospheric modeling. *Methods Comput. Phys.*, **17,** 268–324.

Coiffier, J., Y. Ernie, J.-F. Geleyn, J. Clochard and F. Dupont, 1986: The operational hemispheric model at the French Meteorological Service. *WMO/IUGG International Symposium on Short- and Medium-Range NWP,* Tokyo, World Meteor. Org., WMO Tech. Doc. 114, 265–268.

Chessman, G. P., 1960: Improved terrain effects in barotropic forecasts. *Mon. Wea. Rev.*, **88,** 327–342.

Daley, R., C. Girard, J. Henderson and I. Simmonds, 1976: Short-term forecasting with a multi-level spectral primitive equation model. *Atmosphere,* **14,** 98–116.

Deardorff, J. W., 1978: Efficient prediction of ground surface temperature and moisture with inclusion of a layer of vegetation. *J. Geophys. Res.*, **83,** 1889–1903.

Geleyn, J.-F., 1980: Some diagnostics of the cloud-radiation interaction on ECMWF forecasting model. *ECMWF Workshop on Radiation and Cloud-Radiation Interaction in Numerical Modelling,* Reading, 135–162. [Available from ECMWF, Shinfield Park, Reading, Berkshire RG2 9AX, England.]

Kalnay, E., and M. Kanamitsu, 1988: Time schemes for strongly nonlinear damping equations. *Mon. Wea. Rev.*, **116,** 1945–1958.

Kaplan, M. L., J. W. Zack, V. C. Wong and J. J. Tuccillo, 1982: Initial results from a mesoscale atmospheric simulation system and comparisons with the AVE–SESAME I dataset. *Mon. Wea. Rev.*, **110,** 1564–1590.

Keyser, D., and L. W. Uccellini, 1987: Regional models: emerging research tools for synoptic meteorologists. *Bull. Amer. Meteor. Soc.*, **68,** 306–320.

Koch, S., W. C. Skillman, P. J. Kocin, P. J. Wetzel, K. F. Brill, D. A. Keyser and M. C. McCumber, 1985: Synoptic scale forecast skill and systematic errors in the MASS 2.0 model. *Mon. Wea. Rev.*, **113,** 1714–1737.

Kondo, J., 1971: Effect of radiative heat transfer on profiles of wind, temperature and water vapor in the atmospheric boundary layer. *J. Meteor. Soc. Japan,* **49,** 75–94.

Louis, J. F., 1984: *ECMWF Forecast Model Physical Parameterization Research Manual 3.* [Available from ECMWF, Shinfield Park, Reading, Berkshire RG2 9AX, England.]

Machenhauer, B., and J. E. Haugen, 1987: Test of a spectral limited area shallow water model with time-dependent lateral boundary conditions and combined normal mode/semi-Lagrangian time integration schemes. *ECMWF Workshop on Techniques for Horizontal Discretization in Numerical Weather Prediction Models,* Reading, 361-377. [Available from ECMWF, Shinfield Park, Reading, Berkshire RG2 9AX, England].

Mailhot, J., and R. Benoit, 1982: A finite-element model of the atmospheric boundary layer suitable for use with numerical weather prediction models. *J. Atmos. Sci.*, **39,** 2249–2266.

——, and C. Chouinard, 1989: Numerical forecasts of explosive winter storms: sensitivity experiments with a meso-α scale model. *Mon. Wea. Rev.*, **117,** 1311–1343.

Orlanski, I., and J. J. Katzfey, 1987: Sensitivity of model simulations for a coastal cyclone. *Mon. Wea. Rev.*, **115,** 2792–2821.

Sasamori, T., 1972: A linear harmonic analysis of atmospheric motion with radiative dissipation. *J. Meteor. Soc. Japan,* **50,** 505–518.

Simmons, A. J., B. J. Hoskins and D. M. Burridge, 1978: Stability of the semi-implicit method of time integration. *Mon. Wea. Rev.*, **106,** 405–412.

Staley, D. O., and G. M. Jurica, 1972: Effective atmospheric emissivity (under clear skies). *J. Appl. Meteor.*, **11,** 349–356.

Staniforth, A. N., and R. W. Daley, 1977: A finite-element formulation for the vertical discretization of sigma-coordinate primitive equation models. *Mon. Wea. Rev.*, **105,** 1108–1118.

——, and H. L. Mitchell, 1977: A semi-implicit finite-element barotropic model. *Mon. Wea. Rev.*, **105,** 154–169.

——, and ——, 1978: A variable-resolution finite-element technique for regional forecasting with the primitive equations. *Mon. Wea. Rev.*, **106,** 439–447.

——, and R. W. Daley, 1979: A baroclinic finite-element model for regional weather forecasting with the primitive equations. *Mon. Wea. Rev.*, **107,** 107–121.

——, and J. Mailhot, 1988: An operational model for regional weather forecasting. *Comput. Math. Applic.*, **16,** 1–22.

Temperton, C., 1988: Implicit normal mode initialization. *Mon. Wea. Rev.*, **116,** 1013–1031.

Uccellini, L. W., D. Keyser, K. F. Brill and C. H. Wash, 1985: The Presidents' Day Cyclone of 18–19 February 1979: Influence of upstream trough amplification and associated tropopause folding on rapid cyclogenesis. *Mon. Wea. Rev.*, **113,** 962–988.

——, R. A. Petersen, K. F. Brill, P. J. Kocin and J. T. Tuccillo, 1987: Synergistic interactions between an upper-level jet streak and diabatic processes that influence the development of a low-level jet and a secondary coastal cyclone. *Mon. Wea. Rev.*, **115,** 2227–2261.

Verner, G., and R. Benoit, 1984: Normal mode initialization of the RPN finite-element model. *Mon. Wea. Rev.*, **112,** 1535–1543.